European Journal of Medicinal Chemistry 279 (2024) 116909

Contents lists available at ScienceDirect

European Journal of Medicinal Chemistry

journal homepage: www.elsevier.com/locate/ejmech

Research paper

Novel tris-bipyridine based Ru(II) complexes as type-I/-II photosensitizers for antitumor photodynamic therapy through ferroptosis and immunogenic cell death

Hongwei Zheng [a,b,1], Kai Wang [b,1], Dongliang Ji [a,b,1], Xiao Liu [a,b], Chen Wang [a,b], Yangyang Jiang [b], Zihan Jia [b], Biao Xiong [b,***], Yong Ling [a,b,**], Jiefei Miao [a,b,*]

[a] Department of Oncology, Department of Pharmacy, Affiliated Hospital of Nantong University, Nantong 226001, China
[b] School of Pharmacy and Jiangsu Province Key Laboratory for Inflammation and Molecular Drug Target, Nantong Key Laboratory of Small Molecular Drug Innovation, Nantong University, Nantong 226001, China

ARTICLE INFO

Handling Editor: Dr. Z Liu

Keywords:
Ru(II) complexes
Tris-bipyridine
Photodynamic therapy (PDT)
Antitumor activity
Ferroptosis

ABSTRACT

Ru(II) complexes have attracted attention as photosensitizers for their promising photodynamic properties. Herein, novel tris-bipyridine based Ru(II) complexes (**6a-e**) were synthesized by introducing saturated heterocycles to improve photodynamic properties and lipid-water partition coefficients. Among them, **6d** demonstrated significant phototoxicity towards three cancer cells, with IC_{50} values of 5.66–7.17 μM, exceeding values in dark (IC_{50}s > 100 μM). Under hypoxic conditions, **6d** maintained excellent photodynamic activity in A549 cells, with PI values exceeding 24, highlighting its potential for highly effective type-I/-II photodynamic therapy by inducing ROS generation, oxidative stress, and mitochondrial damage. Additionally, it induced ferroptosis and immunogenic cell death of A549 cells by regulating the expression of relevant markers. Finally, **6d** remarkably inhibited the growth of A549 transplanted tumor growth by 95.4 %. This Ru(II) complex shows great potential for cancer treatment with its potent photodynamic activity and diverse mechanisms of tumor cell death.

1. Introduction

The ongoing battle against cancer remains a paramount concern in global public health, marked by its persistently high morbidity and mortality rates [1–3]. Among the array of malignancies, lung cancer stands out as particularly daunting, often diagnosed at advanced stages where conventional treatments like surgery and radiation become ineffective [4,5]. Furthermore, its intrinsic or acquired multidrug resistance complicates therapeutic interventions, necessitating exploration of alternative modalities [6,7].

In recent decades, photodynamic therapy (PDT) has emerged as a promising avenue for the treatment of certain forms of tumors, including lung cancer, colorectal cancer (CRC), melanoma, and so on [8,9]. This method leverages reactive oxygen species (ROS) generated upon light activation to induce apoptosis, necrosis, vascular damage, and immune responses. PDT offers distinct advantages over traditional methods, including precise spatio-temporal control, non-resistance, and minimal invasiveness [10]. In cases where surgery is not an option or other treatments have failed or been declined, PDT can serve as an option or as part of combination therapy.

Three essential non-toxic components are involved in the process of PDT: the photosensitizers (PSs), laser light of specific wavelengths, and oxygen [11]. Through photochemical reactions, PSs generate toxic ROS to destroy tumor cells. Notably, while type II photochemical reactions (which generate $^1O_2$) dominate current research, type I reactions (which generate $\bullet O_2^-$ and •OH, etc.) are less dependent on oxygen and hold more promise for enhanced therapeutic outcomes in hypoxic tumor microenvironments [12–14]. Therefore, it is of great significance to explore type I/II photosensitizers, which can overcome tumor hypoxia.

The quest for optimal PSs has indeed been a long-standing endeavor,

* Corresponding author. Department of Oncology, Department of Pharmacy, Affiliated Hospital of Nantong University, Nantong 226001, China.
** Corresponding author. Department of Oncology, Department of Pharmacy, Affiliated Hospital of Nantong University, Nantong, 226001, China.
*** Corresponding author. School of Pharmacy and Jiangsu Province Key Laboratory for Inflammation and Molecular Drug Target, Nantong Key Laboratory of Small Molecular Drug Innovation, Nantong University, Nantong 226001, China.
E-mail addresses: hsiung1987@ntu.edu.cn (B. Xiong), LYYY111@sina.com (Y. Ling), miaojfntu@163.com (J. Miao).
[1] These authors contributed equally.

https://doi.org/10.1016/j.ejmech.2024.116909
Received 29 June 2024; Received in revised form 15 September 2024; Accepted 23 September 2024
Available online 24 September 2024

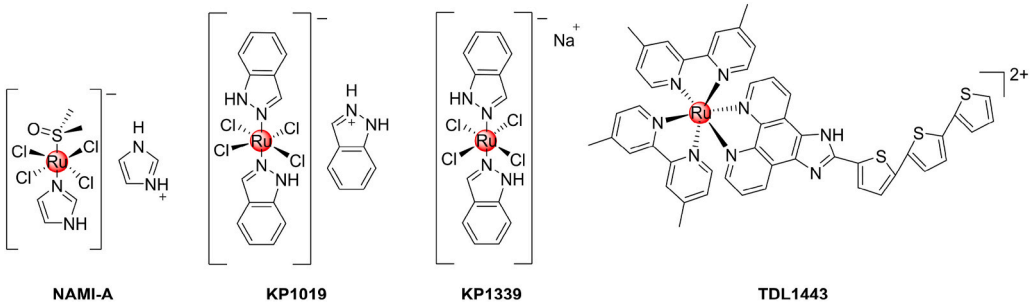

Fig. 1. The chemical structure of four clinical Ru complexes: NAMI-A, KP1019, KP1339, and TLD1443.

tracing back to the pioneering breakthrough of haematoporphyrin derivative (HpD) in the 1960s [15,16]. The tetrapyrrole-based photosensitizers, such as porphyrins, chlorins, and phthalocyanines, stand out as the most extensively researched class of photosensitizers, with certain members already receiving clinical approval [17,18]. However, because of the similar structure core, they often suffer from inherent limitations related to solubility, photostability, pharmacokinetics, and so on [19–21]. In contrast, metal-based drugs, particularly certain Ru complexes, present an extensive array of biological applications, with significant promise in PDT [22,23]. Unlike the flat quadrilateral arrangement in cisplatin, Ru complexes display a d^6 hexa-coordinated octahedral structure with a 3D arrangement of ligands, considerably widening the possibilities for modification [24]. The reasonable choice of ligands can endow Ru complexes with a wide range of superior properties, encompassing the improvement of solubility, photodynamic characteristics, ROS yield, and so on [25,26]. Several Ru complexes have entered clinical research and shown potential for tumor therapy (Fig. 1). NAMI-A and KP1019 have been excluded from clinical use due to their poor anti-tumor effects, limited water solubility, and severe side effects [27,28]. To address the low water solubility of KP1019, researchers have developed a more soluble sodium salt complex, KP1339, which is currently undergoing Phase 1/2 clinical trials for the treatment of various types of tumors [29]. The mentioned three complexes are utilized as chemotherapy agents. Notably, the inert Ru(II) polypyridyl complex TLD1433, pioneered by McFarland et al., has advanced to Phase IB clinical trials for PDT in bladder carcinoma treatment, underscoring the translational potential of Ru(II) complexes [30,31]. Therefore, the development of Ru(II) complexes for PDT holds significant clinical value in cancer therapy.

Given that bipyridine is an important bidentate ligand with good planarity and high designability, its molecular optical and physical properties can be optimized by structural modification. Researches have shown that complexes formed with polypyridine ligands have the ability to emit fluorescence persistently, display remarkable large Stokes shifts, showcase notable single and two-photon absorption abilities, and uphold fluorescence stability under physiological conditions [32–34]. These combined features bestow upon Ru(II) polypyridine complexes the potential for effective photosensitization, a crucial mechanism in PDT. Herein, we employed 4,4′-dimethyl-2,2′-bipyridine as the bidentate ligand parent nucleus and introduced saturated heterocycles to improve the lipid-water partition coefficients (log P) and photodynamic activities, resulting in the novel bidentate nitrogen ligand, bipyridine derivatives **5a-e**. Finally, they were direct coordinated to the Ru metal center to obtain functional tris-bipyridine Ru(II) complexes **6a-e**, enabling facile large-scale synthesis (Fig. 2). It is expected to enhance their photodynamic activities while also improving log P values to promote cellular absorption. Moreover, their potential inhibitory and/or damaging effects on tumor cells through PDT, along with preliminary mechanisms such as cell ferroptosis and immunogenic cell death, were further explored.

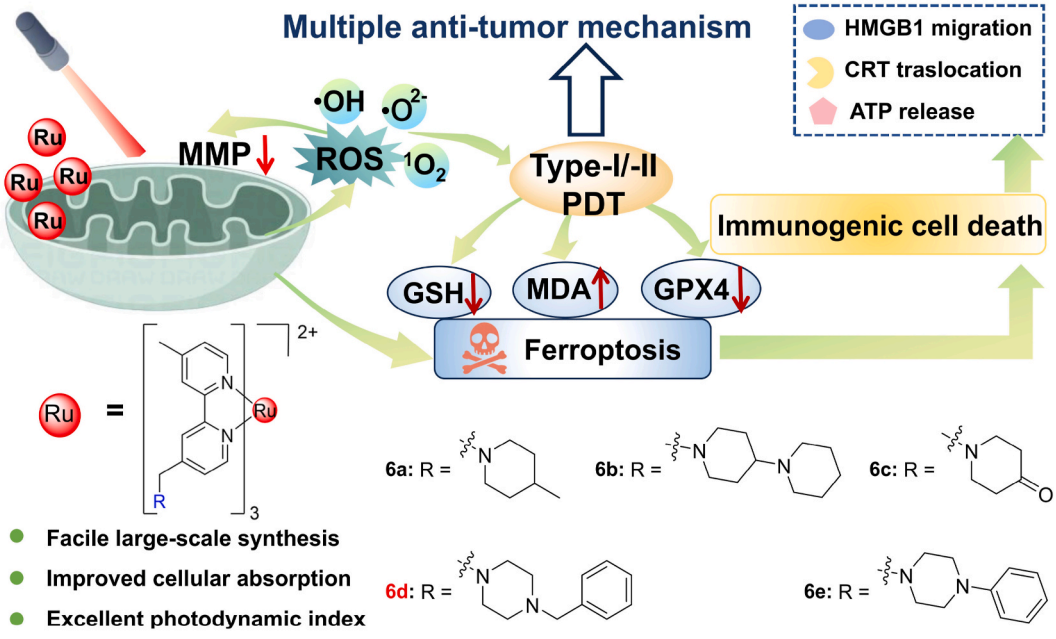

Fig. 2. The chemical structure of novel Ru(II) complexes **6a-e** and the multifaceted mechanisms.

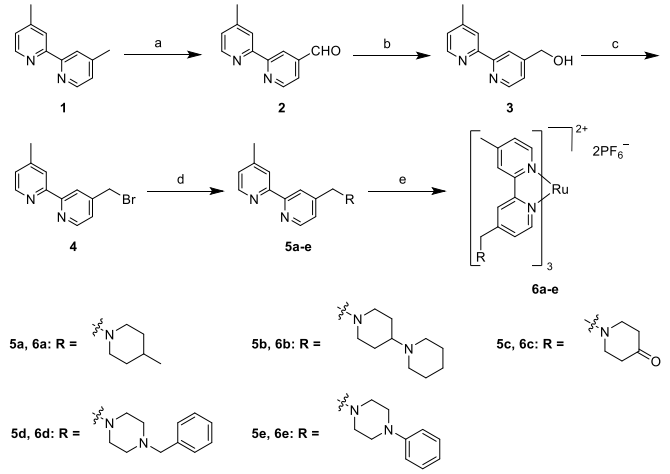

Scheme 1. Synthetic scheme for Ru(II) complexes 6a-e[a]

[a](a) SeO_2, 1,4-dioxane, 100 °C, 24 h, 40 %; (b) $NaBH_4$, MeOH, r. t., 2 h, 88 %; (c) HBr, H_2SO_4, 110 °C, 12 h, 85 %; (d) diverse saturated heterocycles, K_2CO_3, MeCN, 85 °C, 12 h, 71–83 %; (e) $RuCl_3{\cdot}H_2O$, $(CH_2OH)_2$, 120 °C, 6 h, and then NH_4PF_6, three steaming water, r. t., 10 min, 51–57 %.

2. Results and discussion

2.1. Synthesis and characterization

Herein, 4,4′-dimethyl-2,2′-bipyridine was selected as the parent nucleus for the bidentate ligand, and saturated heterocycles were introduced to enhance the log P. The synthesis of Ru(II) complexes **6a-e** is described in Scheme 1. Starting with 4,4′-dimethyl-2,2′-bipyridine (**1**), it was oxidized using selenium dioxide (SeO_2) to yield compound **2**. Subsequent reduction with sodium borohydride ($NaBH_4$) afforded compound **3**. After bromination with phosphorus tribromide (PBr_3), the resulting compound **4** was obtained. Next, various nitrogen heterocycles were introduced to compound **4** to obtain novel bidentate nitrogen ligands **5a-e**. These generated ligands were then coordinated to the metal center of $RuCl_3$, and ammonium hexafluorophosphate (NH_4PF_6) was added to yield the corresponding salts, leading to the formation of Ru(II) complexes **6a-e**. The synthesized compounds were characterized using ^1H and ^{13}C NMR spectroscopy, and ESI-HRMS as described in the Supporting Information (Fig. S11−40).

2.2. Photophysical and photodynamic properties

The UV–visible absorption and fluorescence spectra of Ru(II) complexes **6a-e** were recorded at room temperature, using methanol as the solvent, to investigate their photophysical characteristics. All five complexes exhibited a comparable profile, indicating that the available electronic transitions, as well as the ground and excited states within the complexes, were qualitatively alike (Fig. 3a). They displayed broad peaks spanning the wavelength range of 400–500 nm (with maxima at approximately 459 nm) ascribed to the Metal-to-Ligand Charge Transfer (MLCT) from Ru (dπ) to the bpy ligand (π*) transitions. Moreover, all complexes except for **6b** displayed a high molar extinction coefficient ($>10^4$ M^{-1} cm^{-1}), rendering them highly attractive as photosensitizers for PDT (Table 1). Under ambient conditions, **6a-e** displayed red emission with a peak wavelength approximately 622 nm upon excitation at 459 nm (Fig. 3b).

Firstly, the generation of total ROS by **6a-e** was assessed using 2′,7′-dichlorofluorescin (DCFH, ROS probe), the fluorescence attenuation curves indicated that all five complexes could generate a significant amount of ROS upon irradiation (Fig. 3c and S1). PDT can trigger cancer cell apoptosis via two distinct pathways based on the ROS generated: the type I pathway (electron transfer process) produces $\bullet O_2^-$, •OH, and so on, while the type II pathway (energy transfer process) yields $^1O_2$. The majority of reported PSs are based on type II mechanism, which is greatly relying on oxygen [11]. Dihydroethidium (DHE), 4-hydroxyphenyl-fluorescein (HPF), and 1,3-Diphenylisobenzofuran (DPBF) were utilized to further probe the ability of the five complexes to generate $\bullet O_2^-$, •OH, and $^1O_2$, aiming to identify their specific photodynamic pathways (Fig. 3d−f and S2−4). The fluorescence intensity of DHE and HPF exhibited varying increases upon irradiation, reflecting the different $\bullet O_2^-$ and •OH generation capability of **6a-e**. As an indirect method, the absorbance of DPBF at 415 nm significantly decreased after incubation with **6a-e** followed by exposure to 520 nm light, and the $^1O_2$ quantum yields (Φ_Δ) of **6a-e** was subsequently calculated using [Ru(bpy)$_3$](PF$_6$)$_2$ (RuB) as a reference [35]. As illustrated in Table 1, the results indicate that the $^1O_2$ generation capability of **6a-e** follows this order: **6a** ($\Phi_\Delta = 0.83$) > **6d** ($\Phi_\Delta = 0.81$) > **6e** ($\Phi_\Delta = 0.77$) > **RuB** ($\Phi_\Delta = 0.73$) > **6c** ($\Phi_\Delta = 0.57$) > **6b** ($\Phi_\Delta = 0.23$).

Combining the subsequent phototoxicity data (Table 2), complexes **6d** and **6a** were chosen for the subsequent studies. In the context of photosensitizers, good photostability is deemed to be a crucial prerequisite. Therefore, the photostability of **6d** and **6a** was assessed upon continuous irradiation (520 nm, 200 mW/cm^2) in methanol and monitoring of the potential conversion of the complexes by UV–visible absorption spectra. Promisingly, no significantly decrease was observed, indicative of the high photostability of them (Fig. S5). Moreover, the relative fluorescence quantum yields of **6a** and **6d** were assessed in a mixed solution of methanol and ethanol (1:4, v/v) using RuB as the reference ($\Phi_F = 0.328$) [36]. **6d** demonstrated a higher fluorescence quantum yield of 0.329, surpassing that of **6a** which stands at 0.273.

Electron spin resonance (ESR) spectroscopy was employed to further confirmed the $\bullet O^{2-}$ and $^1O_2$ generation ability of **6d**. 5,5-dimethyl-1-pyrroline N-oxide (DMPO) and 2,2,6,6-tetramethyl-4-piperidone (TEMP) were employed as the $\bullet O_2^-$ and $^1O_2$ trapping agents, respectively. Clearly, a strong characteristic signal of $\bullet O_2^-$ was detected in the methanol solution of **6d** under 520 nm illumination. No apparent $\bullet O_2^-$ signal was observed in the absence of light (Fig. 3g). These results are consistent with the DHE fluorescence attenuation curves, confirming that $\bullet O_2^-$ was generated only when **6d** was under photoexcitation (Fig. 3d). Interesting, complex **6d** exhibited notably reduced •OH production compared to $\bullet O_2^-$, implying its reliance primarily on $\bullet O_2^-$ to mediate type I PDT (Fig. 3e and h). The characteristic triplet ESR signal of $^1O_2$ was also observed after 520 nm irradiation (Fig. 3i). Taken together, these findings imply that further mechanism investigation into photodynamic activity of **6d** was worthwhile due to its significant potential as a potent generator of ROS through both type I and type II processes.

2.3. In vitro phototoxicity

We conducted further toxicity evaluations of **6a-e** under both dark condition and irradiation against various cell lines, including HT29 human colon cancer cells, A549 human lung cancer cells, and 4T1 mouse breast cancer cells. The cell inhibition rates of all complexes at varying concentrations are depicted in Fig. 4 and S6-7, while the resulting IC_{50} values and photocytotoxicity indices (PI) of **6a-e** are calculated and presented in Table 2. It is evident that among all complexes, the dark toxicity of **6d** to these cell lines was minimal in both under normoxic and hypoxic conditions (IC_{50}s > 100 μM) (Table S1). However, under 520 nm photoirradiation, the photocytotoxicity of **6d** increased significantly (IC_{50}s = 4.16–9.12 μM), with PI all exceeding 10.9. Interestingly, **6d** demonstrated higher photocytotoxicity against HT29 and A549 cells in hypoxia, indicating its ability to overcome the limitation of O_2 concentration through type I and type II photodynamic reactions. These experimental results further validate our previous experiments and attest to the potential of complex **6d** to serve as a type-I/-II photosensitizer.

The partition coefficient between lipid and water affects the

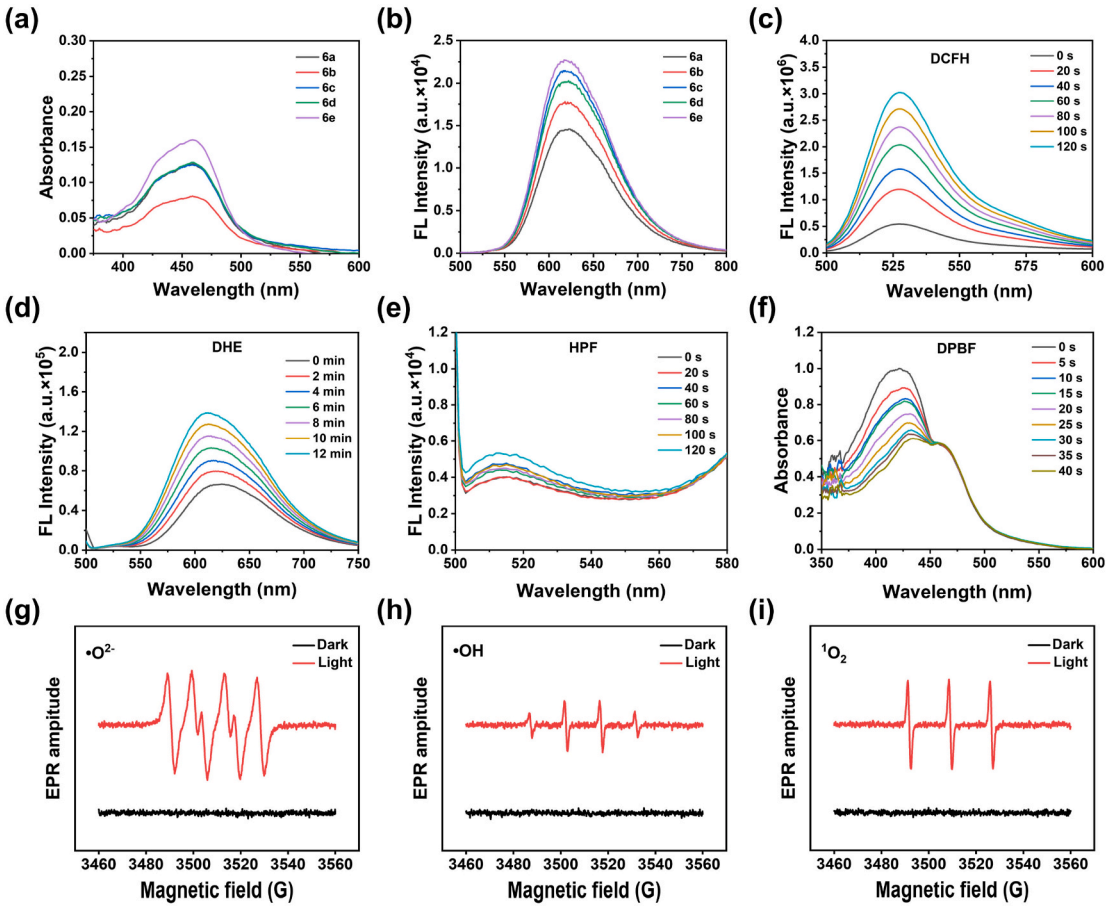

Fig. 3. Photophysical and photodynamic properties of Ru complexes **6a-e**. UV–Vis absorption (a) and fluorescence (b) spectra of **6a-e** (10 μM) measured in methanol solution at room temperature, λ_{ex} = 460 nm. (c) The fluorescence changes of **6d** (10 μM) in methanol solution containing DCFH (total ROS probe) under laser irradiation. (d) The fluorescence changes of **6d** (10 μM) in methanol solution containing DHE ($\bullet O_2^-$ probe) under laser irradiation. (e) The fluorescence changes of **6d** (10 μM) in methanol solution containing HPF (•OH probe) under laser irradiation. (f) The absorption attenuation curve of DPBF measured in methanol solution of **6d** under laser irradiation. EPR signals for the $\bullet O_2^-$ (g), •OH (h), and $^1O_2$ (i) characterization of **6d** upon irradiation or in the dark. Light dose: 520 nm, 200 mW/cm^2.

Table 1
The log P values measured by the classical shake-flask method and photophysical properties of complexes **6a–e**.

Compd.	λ_{abs} (nm)	ε (M^{-1} cm^{-1})	λ_{em} (nm)	stokes shift (nm)	Φ_Δ	Φ_F	log P
RuB	456	16,200	609	153	0.73	0.328	−1.91 ± 0.21
6a	459	12,607	623	164	0.83	0.273	0.35 ± 0.02
6b	459	8085	618	159	0.23	NC[a]	−2.51 ± 0.01
6c	459	12,460	618	159	0.57	NC	−1.33 ± 0.05
6d	459	12,814	622	163	0.81	0.329	0.04 ± 0.02
6e	459	16,027	617	158	0.77	NC	0.50 ± 0.07

[a] NC: not calculated.

distribution, efficacy, and safety of drugs in the body. Improving the partition coefficient could potentially enhance cellular uptake and increase the effectiveness of anticancer drugs. The log P of complexes **6a-e** have been calculated and listed in Table 1, with values of 0.35, −2.51, −1.33, 0.04, and 0.50, four of which were higher than RuB (log P = −1.91), indicating easier cellular entry. Inspired by the excellent photodynamic properties and phototoxicity of complexes **6a**, **6d**, and **6e**, flow cytometry was employed to evaluate their uptake by A549 tumor cells. Initially, we investigated the cellular internalization of **6d** at various time points and observed maximal uptake at 2 h, which then slightly decreased by 4 h (Figs. S8a and b). Subsequently, comparison of the internalization of the three complexes at 2 h revealed that **6d** exhibited significantly more and faster cellular uptake, approximately 5.8 times that of the positive control RuB (Figs. S8c and d). Combining with the log P of the three complexes, **6d** maintained a moderate value, which may account for its favorable cellular uptake behavior.

The selective phototoxic effect of **6d** against A549 cells was also further visually evaluated by the live and dead cell staining with calcein-AM and propidium iodide (PI) dyes. Obviously, only irradiation or **6d** itself failed to cause a certain amount of cell death. However, **6d** upon irradiation could induce cell death efficiently, indicated by the appearance of red fluorescence from PI (Fig. 5c). Similar experimental results were observed in the **6a**-treated 4T1 cells (Fig. 5a). Notably, **6d** group exhibited a substantial reduction in the red/green fluorescence ratio from 7.67 to 0.89 between the dark and light conditions, whereas the **6a** group decreased from 12.08 to 0.32 (Fig. 5b and d).

Table 2
IC_{50} values in the dark or under irradiation of complexes **6a-e** toward three cancer cell lines.

Compd.	Conditions		*In vitro* antiproliferative activity (IC_{50}, μM)		
			HT29	A549	4T1
RuB	normoxia[a]	Dark	>100	>100	>100
		Light	14.90 ± 1.70	27.90 ± 1.30	95.62 ± 16.16
		PI[d]	>6.71	>3.58	>1.05
6a	normoxia	Dark	>100	>100	84.53 ± 8.88
		Light	8.01 ± 0.67	9.39 ± 0.45	11.22 ± 0.36
		PI	**> 12.48**	**> 10.65**	7.53
6b	normoxia	Dark	>100	>100	69.59 ± 5.41
		Light	27.30 ± 2.46	22.61 ± 1.48	20.06 ± 0.10
		PI	>3.66	>4.42	3.47
6c	normoxia	Dark	>100	>100	>100
		Light	>100	>100	>100
		PI	NC[c]	NC	NC
6d	normoxia	Dark	>100	>100	>100
		Light	5.78 ± 1.86	5.66 ± 0.53	7.17 ± 0.51
		PI	**> 17.30**	**> 17.67**	**> 13.95**
6d	hypoxia[b]	Dark	>100	>100	>100
		Light	5.09 ± 0.41	4.16 ± 0.18	9.12 ± 0.25
		PI	**> 19.65**	**> 24.04**	**> 10.96**
6e	normoxia	Dark	>100	>100	>100
		Light	5.88 ± 0.21	7.90 ± 0.04	9.99 ± 1.59
		PI	**> 17.00**	**> 12.66**	**> 10.01**

[a] Cytotoxicity of the tested compound incubated for 24 h in normoxia (21 % O_2).
[b] Cytotoxicity of the tested compound incubated for 24 h in hypoxia (1 % O_2).
[c] NC: not calculated.
[d] PI: phototoxic indices, $IC_{50,\ dark}/IC_{50,\ irradiation}$. Irradiation: 520 nm, 200 mW/cm^2, 10 min.

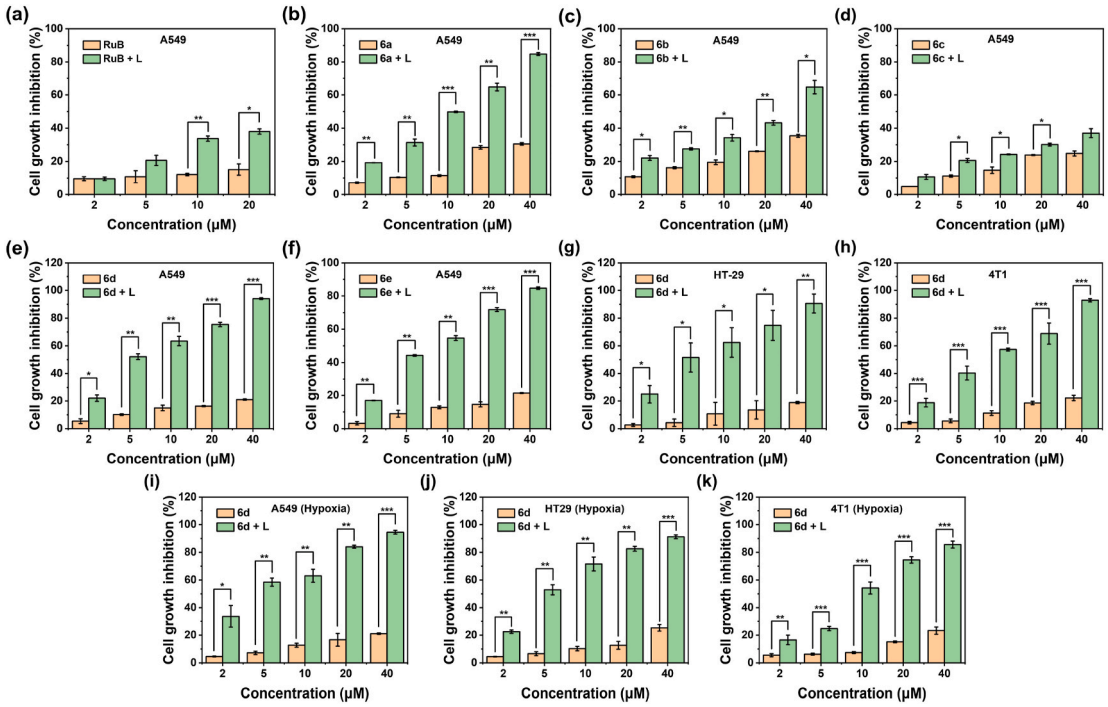

Fig. 4. Cytotoxicity and phototoxicity of RuB (a), **6a** (b), **6b** (c), **6c** (d), **6d** (e), and **6e** (f) against A549 cells in normoxia incubated for 24 h with/without irradiation. Cytotoxicity and phototoxicity of **6d** against HT29 (g) and 4T1 (h) cells in normoxia, and against A549 (i), HT29 (j), and 4T1 (k) cells in hypoxia incubated for 24 h with/without irradiation. L: Light. Light dose: 520 nm, 200 mW/cm^2, 10 min. The related data are presented as the means ± SD of three separate assays, n = 3. (*, $P < 0.05$; **, $P < 0.01$; ***, $P < 0.001$).

2.4. Subcellular localization studies

The subcellular localization of **6d** in A549 cells was determined by confocal laser scanning microscopy (CLSM). As depicted in Fig. 6, the red fluorescence emitted by **6d** exhibited a significant overlap with the green fluorescence channels of the commercial mitochondrial dye Mito-Tracker Green and lysosomal dye Lyso-Tracker Green, with a Pearson's correlation coefficient (PCC) of 0.83 and 0.85, respectively. Similarly, we investigated the subcellular distribution of **6a** in 4T1 cells. Microscopic images demonstrated a notable correlation with PCC values of 0.85 and 0.81 with Mito-Tracker Green and Lyso-Tracker Green, respectively. These experimental results indicate mitochondria and lysosomal as the primary localization of the Ru(II) complexes we designed.

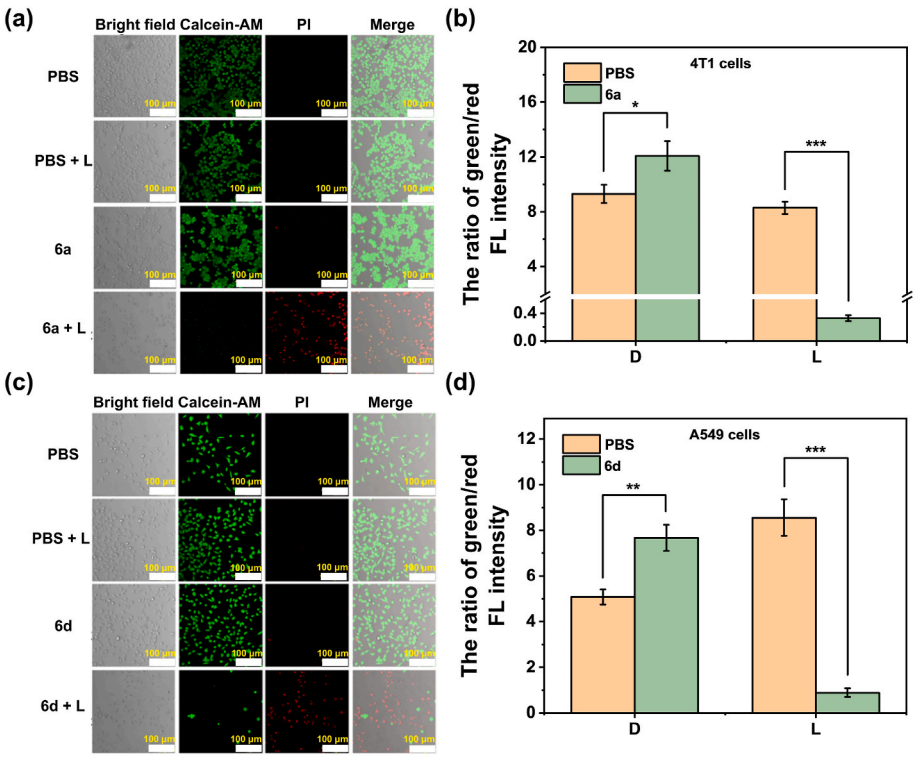

Fig. 5. (a) CLSM images of 4T1 cells upon incubation with **6a** (10 μM) and calcein-AM (live, green)/PI (dead, red) in the dark or upon irradiation. (b) Ratio of green/red fluorescence intensity of (a). (c) CLSM images of A549 cells upon incubation with **6d** (10 μM) and calcein-AM (live, green)/PI (dead, red) in the dark or upon irradiation. (d) Ratio of green/red fluorescence intensity of (c). D: Dark; L: Light. Light dose: 520 nm, 200 mW/cm^2, 10 min. Scale bar: 100 μm. The related data are presented as the means ± SD of three separate assays. (*, $P < 0.05$; **, $P < 0.01$; ***, $P < 0.001$).

2.5. Intracellular ROS generation

Considering the remarkable phototoxicity performed by **6a** and **6d**, we postulated that this effect might be attributed to their ability to induce a substantial amount of ROS. The intracellular ROS levels induced by complexes **6a** and **6d** were examined through 2,7-dichlorofluorescin diacetate (DCFH-DA) fluorescence assay measured by confocal microscopy. DCFH-DA is a non-fluorescent dye that can be enzymatically hydrolyzed and oxidized by ROS to form fluorescent dichlorofluorescein (DCF), emitting a green fluorescence. The fluorescence images disclosed that a significantly higher intensity (3.8 times greater than that of the control group) in A549 cells incubated with **6d** upon irradiation. In contrast, negligible green fluorescence was observed in the other groups, which either received light treatment alone or were incubated with only **6d** (Fig. 7c and d). Similar trends were observed in 4T1 cells incubated with **6a**, with a 2.1-fold increase in fluorescence intensity compared to the control group (Fig. 7a and b). These findings unequivocally verify that **6a** and **6d** possess the capability to generate substantial levels of ROS within cells under specific light conditions, thereby validating their excellent phototoxicity.

2.6. Mitochondria damage

The generation of ROS typically results in an imbalance in the cellular redox environment, commonly indicated by damage to the integrity of the mitochondrial membrane [37,38]. Maintaining mitochondrial membrane integrity is crucial for cell survival. Since complexes **6a** and **6d** primarily localize in the mitochondria, their impact on mitochondrial integrity was assessed by monitoring changes in mitochondrial membrane potential (MMP) using the commercial probe JC-1, which selectively stains polarized mitochondria. Mitochondrial depolarization is indicated by a decreased red/green fluorescence intensity ratio (I_{585nm}/I_{530nm}). Both A549 and 4T1 cells showed a decrease in red fluorescence signal and a significant increase in green fluorescence intensity upon illumination after incubation with **6a**/**6d**, respectively (Fig. 8). Notably, the ratio of green to red fluorescence of 4T1 cells and A549 cells increased by 2.44-fold and 3.26-fold, respectively. These findings provide evidence that **6a** and **6d** likely induce cell death by damaging the mitochondria.

Based on the aforementioned experimental findings, it can be inferred that complexes **6a** and **6d** possess the ability to accumulate within mitochondria upon entering tumor cells. Upon light exposure, these complexes generate ROS, leading to mitochondrial dysfunction and triggering tumor cell death, thereby exhibiting the photodynamic therapeutic efficacy.

2.7. The mechanisms of cell death

Ferroptosis, a recently unveiled mode of regulated cell death, is attributed to the buildup of lipid peroxides (LPOs) mediated by intracellular iron, and has garnered increasing attention due to its link with immune responses in tumors [39,40]. The induction of ferroptosis, characterized by the depletion of glutathione (GSH), downregulation of glutathione peroxidase 4 (GPX4), and accumulation of LPOs, is widely recognized as a promising therapeutic strategy in cancer treatment [41–43].

Leveraging knowledge of the mechanisms, the impact of **6d** on these distinctive ferroptosis-associated hallmarks was further explored in A549 cells. Measurement of the GSH level was carried out using Glutathione Assay Kit to evaluated the GSH depletion capability of **6d**. Remarkably, a substantial decrease in GSH levels was observed in A549 cells incubated with **6d** upon irradiation, likely attributed to the

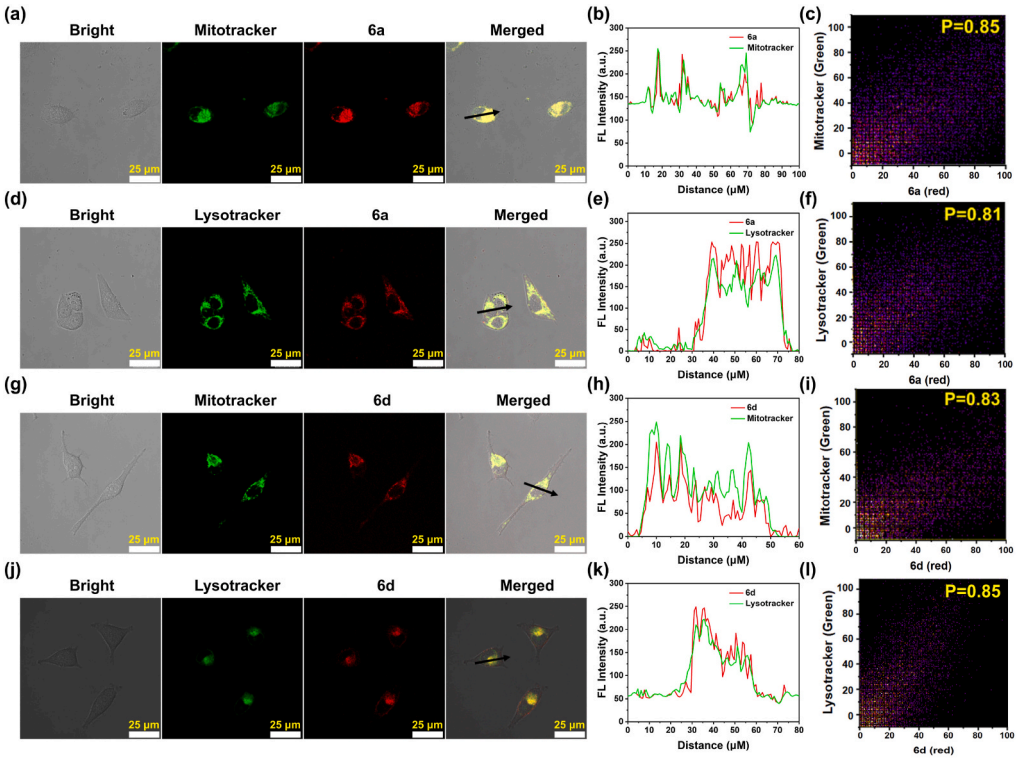

Fig. 6. Subcellular localization of **6a** and **6d**. CLSM images (a) and Z-stack scanning (b) of 4T1 cells after incubated with Mito-Tracker Green (2 μM) and **6a** (10 μM). (c) The Pearson Correlation Coefficient of **6a** and Mito-Tracker Green in 4T1 cells. CLSM images (d) and Z-stack scanning (e) of 4T1 cells after incubated with Lyso-tracker Green (2 μM) and **6a** (10 μM). (f) The Pearson Correlation Coefficient of **6a** and Lyso-tracker Green in 4T1 cells. CLSM images (g) and Z-stack scanning (h) of A549 cells after incubated with Mito-Tracker Green (2 μM) and **6d** (10 μM). (i) The Pearson Correlation Coefficient of **6d** and Mito-Tracker Green in A549 cells. CLSM images (j) and Z-stack scanning (k) of A549 cells after incubated with Lyso-tracker Green (2 μM) and **6d** (10 μM). (l) The Pearson Correlation Coefficient of **6d** and Lyso-tracker Green in A549 cells. Scale bar: 25 μm.

oxidation process catalyzed by ROS. In contrast, the reduction in GSH levels in the remaining experimental groups was almost negligible (Fig. 9a). Previous research has proposed that reduced glutathione levels may impede the expression of GPX4, given that glutathione serves as the intrinsic substrate for GPX4. Subsequent Western blot analysis validated a decrease in GPX4 expression following treatment with **6d** and exposure to light (Fig. 9c). Furthermore, the Lipid Peroxidation MDA Assay Kit was employed to examine the intracellular generation of malondialdehyde (MDA), a crucial end product of lipid peroxidation known for its positive regulatory impact on ferroptosis [44]. While a certain level of MDA was produced upon treatment with **6d** alone, a significant enhancement of the MDA generation was observed upon exposure to light in A549. Specifically, intracellular MDA levels increased by 7.77-fold following treatment with **6d** in conjunction with irradiation, compared to the PBS + light group (Fig. 9b). Notably, the addition of Fer-1 (ferrostatin-1, a ferroptosis inhibitor) effectively alleviated MDA generation. These combined findings provide compelling evidence that the combination of **6d** treatment and exposure to light irradiation induces cell death through the process of ferroptosis. Next, the C11-BODIPY 581/591 probe was employed to measure the level of lipid ROS in A549 cells. It was observed that the cells treated with **6d** exhibited a subtle shift in fluorescence from red to green. However, this trend was significantly enhanced in the light-exposed group, indicating that **6d** under light conditions markedly induces a substantial increase in endogenous lipid ROS levels within the cells (Fig. S9).

Several specific inhibitors were employed to further understand the contribution of ferroptosis in comparison to traditional cell death mechanism (Fig. 9d), including 3-methyladenine (3-MA, an autophagy inhibitor), Fer-1, necrostatin-1 (Nec-1, an inhibitor of necroptosis) and *Z*-VAD-FMK (a pancaspase inhibitor). The pre-incubation with 3-MA and Fer-1 demonstrated significant mitigating effects on cell death induced by treatment with **6d** and exposure to irradiation. Notably, Fer-1 exhibited a more pronounced impact than 3-MA. These findings strongly indicate that **6d** primarily triggers cell demise through the induction of ferroptosis, rather than apoptosis or necrosis.

In consideration of previous research suggesting a potential link between ferroptosis and immunogenic cell death (ICD), we sought to explore the impact of **6d** on this particular mode of cell demise. ICD involves the translocation of endoplasmic reticulum-resident calreticulin (CRT) and heat shock protein 70 (HSP70) to the cell surface, along with the release of adenosine triphosphate (ATP) and the nuclear high-mobility group box 1 (HMGB1) protein [45–47]. These characteristic markers were therefore investigated upon treatment of A549 cells with **6d**.

Utilizing immunofluorescence confocal laser scanning microscopy, we discerned the migration of CRT, as depicted in Fig. 9e. Notably, no discernible alterations were noted following treatment with PBS or DOX. In stark contrast, a notable translocation of CRT to the cytoplasm or cell membrane was evident upon treatment with **6d** and exposure to light, with the CRT ratio reaching 3.9-fold that of the PBS + light group (Fig. 9g). Additionally, the migration of nuclear HMGB1 protein from the nucleus into the extracellular space following treatment with **6d** upon irradiation was confirmed, with the nuclear HMGB1 level decreased to 12.9 % of the PBS + light group (Fig. 9f and h). Subsequently, we investigated the extracellular secretion of ATP using a specific bioluminescence detection kit. Remarkably, a remarkable 5-fold increase in extracellular ATP levels was detected in A549 cells treated with **6d** and subsequently exposed to irradiation, as illustrated in Fig. 9i.

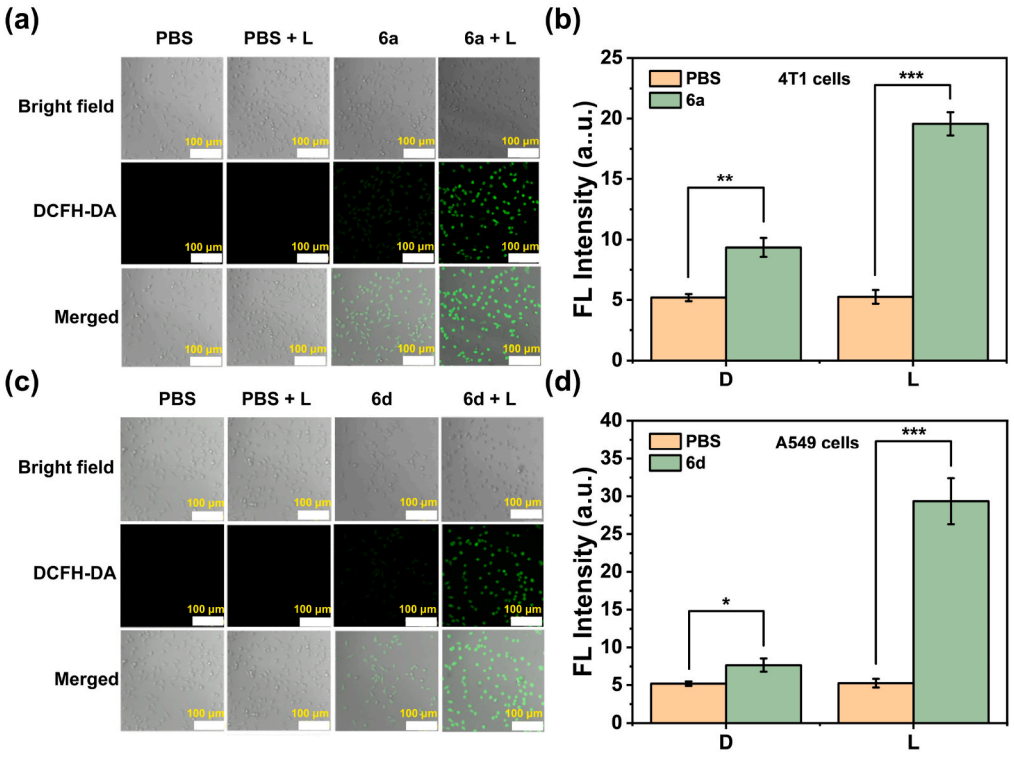

Fig. 7. Intracellular ROS generation by **6a** and **6d**. CLSM images of intracellular ROS levels in 4T1 cells treated with **6a** (10 μM) (a) and A549 cells treated with **6d** (10 μM) (c) with/without a 520 nm laser irradiation (200 mW/cm^2, 10 min). Average fluorescence intensity of DCFH-DA in 4T1 cells (b) and A549 cells (d) of different groups. D: Dark; L: Light. Light dose: 520 nm, 200 mW/cm^2, 10 min. Scale bar: 100 μm. The related data are presented as the means ± SD of three separate assays. (*, $P < 0.05$; **, $P < 0.01$; ***, $P < 0.001$).

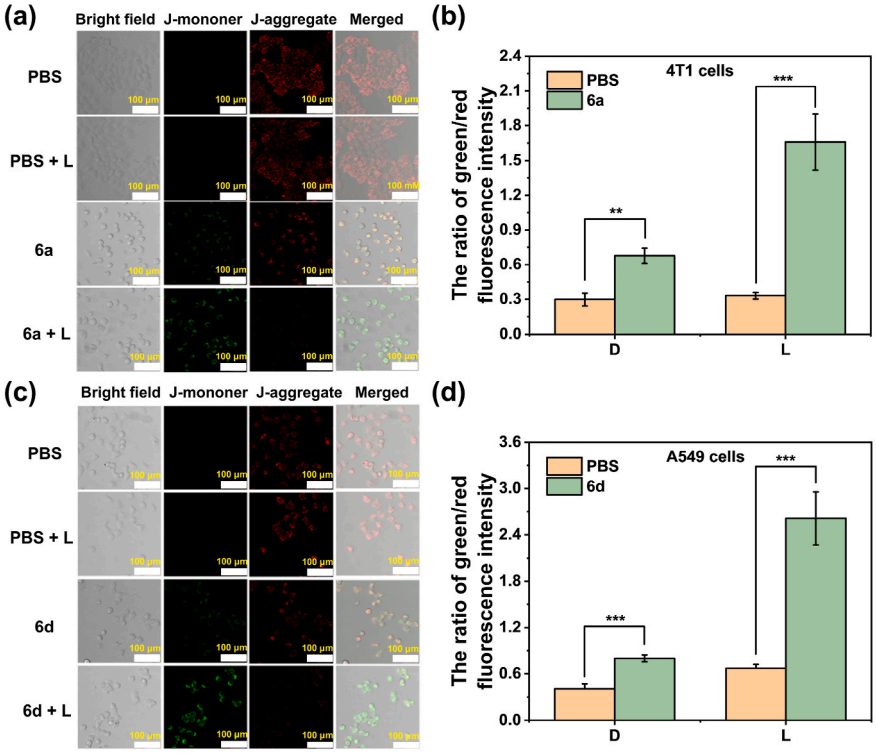

Fig. 8. Induction of Mitochondria Damage by **6a** and **6d**. CLSM images of MMP condition in 4T1 cells treated with **6a** (10 μM) (a) and A549 cells treated with **6d** (10 μM) (c) with/without laser irradiation (520 nm, 200 mW/cm^2, 10 min) measured with JC-1 dye. Ratio of green/red fluorescence intensity of 4T1 cells (b) and A549 cells (d). D: Dark; L: Light. Light dose: 520 nm, 200 mW/cm^2, 10 min. Scale bar: 100 μm. The related data are presented as the means ± SD of three separate assays. (*, $P < 0.05$; **, $P < 0.01$; ***, $P < 0.001$).

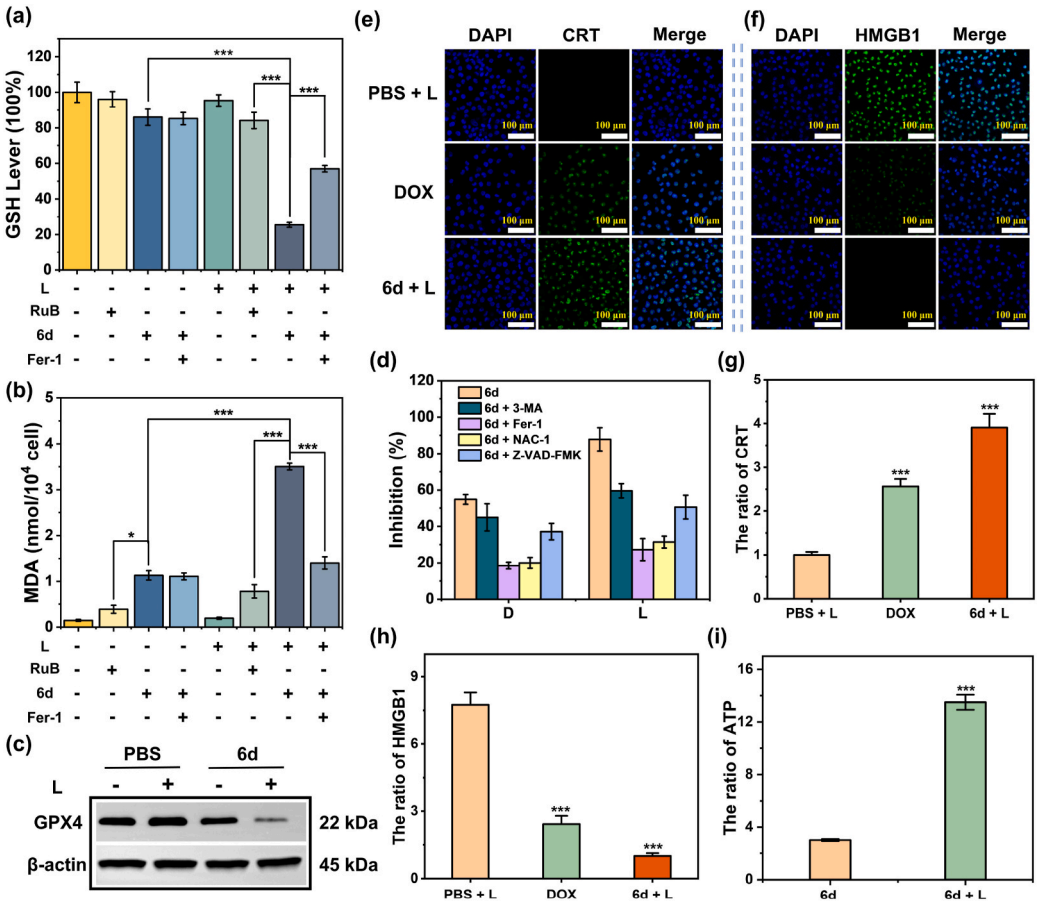

Fig. 9. The mechanisms of cell death induced by **6d**. (a) Intracellular GSH content of A549 cells after treatment with PBS, RuB (10 μM) or **6d** (10 μM) with/without irradiation. (b) Intracellular MDA content of A549 cells after treatment with PBS, RuB (10 μM), **6d** (10 μM) or **6d** (10 μM) + Fer-1 (1 μM) with/without irradiation. (c) Intracellular GPX4 protein levels by Western blotting assay and MDA content for cells treated with **6d**. (d) Cell viabilities of A549 cells after coincubation for 24 h with **6d** (10 μM) in the presence of different inhibitors, including 3-MA (100 μM), Fer-1 (1 μM), Nec-1 (50 μM) and *Z*-VAD-FMK (5 μM) with/without irradiation. Evaluation for hallmarks of ICD in A549 cells upon treatment with DOX (10 μM) and **6d** (10 μM) with/without irradiation. Immunofluorescence confocal laser scanning microscopy stained with (e) calreticulin-specific antibody and (f) HMGB1-specific antibody. (g) Quantized data of (e). (h) Quantized data of (f). (i) Release of ATP into the cell culture supernatant. D: Dark; L: Light. Light dose: 520 nm, 200 mW/cm^2, 10 min. Scale bar: 100 μm. The related data are presented as the means ± SD of three separate assays. (*, $P < 0.05$; **, $P < 0.01$; ***, $P < 0.001$).

Collectively, these findings strongly suggest the potential of **6d** to induce ICD upon light irradiation.

2.8. Antitumor activity in vivo

Given the remarkable *in vitro* performance of **6d**, its antitumor efficacy was further evaluated in A549 tumor-bearing BALB/c nude mice model. Upon the establishment of solid tumors, the mice models were randomly assigned to four groups: Group 1 (PBS only), Group 2 (RuB + light), Group 3 (**6d** only), and Group 4 (**6d** + light), each comprising five nude mice. Six hours following intravenous injection, the mice were either kept in the dark or exposed to irradiation (520 nm, 200 mW/cm^2, 10 min). The tumor volume and body weight of each mouse was measured and recorded every three days over a span of 12 days (Fig. 10a). Under laser irradiation, complex **6d** nearly completely inhibited tumor growth, resulting in a reduction of tumor volume and weight by 85.9 % and 95.36 % respectively, outperforming the rates of RuB + light group (0.79 % and 77.54 %) (Fig. 10b–d). These findings were further supported by isolated tumor images from the different groups, highlighting the potent *in vivo* antitumor efficacy of **6d** (Fig. 10c).

Hematoxylin and eosin (H&E) staining results revealed severe damage to tumor cells in the **6d** + light group, whereas only slightly damage was observed in the RuB + light group (Fig. 10f). No damage or necrosis was detected in the tumor tissues of the remaining two groups. These results validate the remarkable *in vivo* photodynamic therapy and anti-tumor activity of **6d**. Furthermore, the mice exhibited normal behavior without any signs of pain, stress, or discomfort, and the body weight of the **6d** + Light group remained unchanged (Fig. 10e). Consistently, no pathological abnormalities were observed in the H&E staining of vital organs and blood routine indexes, indicating the high biocompatibility of the treatment (Fig. 10f and S10). Utilizing 4T1 murine models and identical methodologies, a parallel assessment was undertaken to evaluate the *in vivo* anti-tumor efficacy and biological safety of **6a**. The outcomes revealed a remarkable suppression of 85.8 % in tumor volume and an impressive 92.73 % reduction in tumor weight (Fig. 10g–l). In conclusion, the research findings demonstrated significant potential for **6d** and **6a** to reduce systemic toxicity and exert anti-

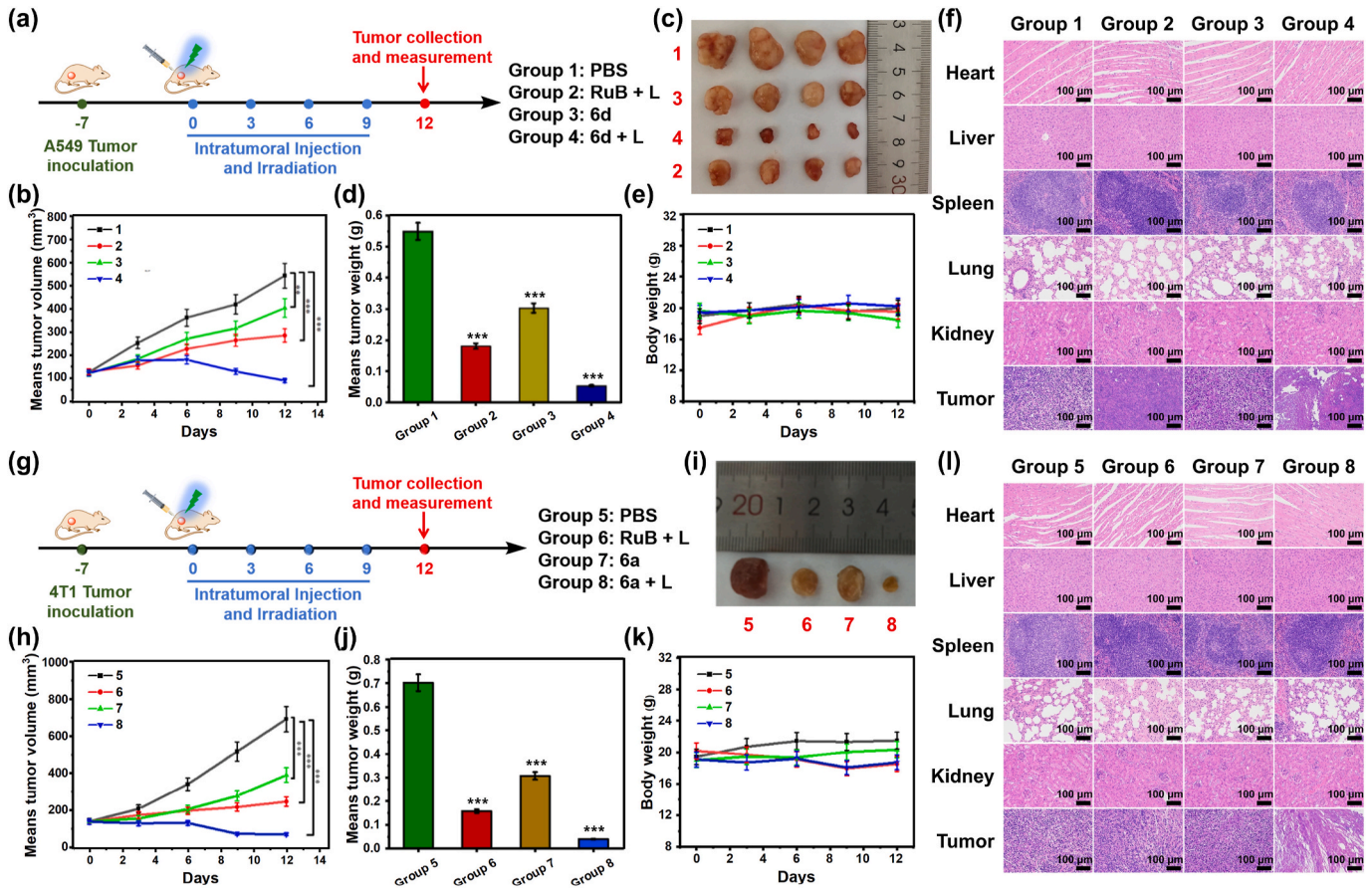

Fig. 10. Evaluation of the treatment in 4T1/A549 tumor-bearing BALB/c nude mice model after intratumor injection of **6a/d** (5 mg/kg) and exposure to irradiation. (a) and (g) Schematic illustration of the treatment. (b) and (h) Tumor growth curves of the tumor-bearing mice during different treatments. (c) and (i) Images of the collected tumors from tumor-bearing mice 12 days after different treatment. (d) and (j) Means tumor weight of mice after different treatments. (e) and (k) Body weights of the mice during different treatments. (f) and (l) Images of H&E staining heart, liver, spleen, lung, kidney and tumor slices from mice after different treatments. L: Light. Light dose: 520 nm, 200 mW/cm^2, 10 min. Scale bar: 100 μm. The related data are presented as the means ± SD of three separate assays. (*, $P < 0.05$; **, $P < 0.01$; ***, $P < 0.001$).

tumor effects through various mechanisms, emphasizing the need for further thorough exploration in future studies.

3. Conclusion

In brief, this article discusses the synthesis of five structurally straightforward Ru(II) metal complexes **6a-e** featuring bipyridyl ligands for PDT, as well as their photo-physicochemical properties. These complexes were found to exhibit a maximum absorption peak at approximately 460 nm, with emission wavelengths extending to 650 nm. Notably, the most promising Ru(II) complex **6d** displayed outstanding photodynamic properties, characterized by a high $^1O_2$ quantum yield and remarkable $\bullet O^{2-}$ generation capacity. It was observed that **6d** demonstrates limited cytotoxicity against various tumor cell lines in the dark. However, when exposed to 520 nm light, its cytotoxic effects are significantly enhanced, achieving an IC_{50} value of 5.66–7.17 μM against three cancer cell lines, with PI exceeding 14. Additionally, **6d** exhibits strong phototoxicity even in hypoxic tumor environments (IC_{50}s = 4.16−9.12 μM), indicating its potential as Type-I/-II photosensitizer. Further mechanistic studies have shown that **6d** significantly increases ROS generation in cells, leading to mitochondrial damage and subsequent ferroptosis. Interestingly, it has been demonstrated that **6d** also induces ICD, triggering the release of damage-associated molecular patterns (DAMPs). *In vivo* experiments further confirmed the high photodynamic activity and anti-tumor efficacy of **6d**. Collectively, the multifaceted mechanisms underscore the promising potential of **6d** as a novel PDT agent for challenging lung cancer.

4. Experimental

4.1. Materials and reagents

All chemical reagents and solvents for synthesis were obtained from qualified reagent supplies (Aladdin, Bidepharm and Meryer) with analytical reagent grade and were used in whole experiment without further purification. All reactions were monitoring in real time by thin-layer chromatography (TLC). Reaction products were isolated and purified by silica gel column chromatography. ^{1}H NMR and ^{13}C NMR spectra were recorded on a Bruker AV 400 M spectrometer with an internal standard (TMS). UV–vis and fluorescence spectra were performed on a Lambda 35 UV–visible spectrophotometer and RF-5301PC fluorescence spectrophotometer, respectively. Confocal imaging of cells was performed using a confocal microscope (ZISS M880, Germany) imaging system. Complexes **6a-e** were checked with high-performance liquid chromatography (HPLC) with a purity of >95 % (Fig. S41−45). Compounds **2–4** were synthesized according literatures [48].

DCFH, DHE, HPF, DPBF were purchased from Bide Pharmatech (China). MTT was purchased from Energy Chemical (China). Calcein AM/PI Double Stain Kit was purchased from were purchased from Yeasen Biotechnology (China). Lyso-Tracker Green and Mito-tracker Green was purchased from Beyotime Biotechnology (China). 2′,7′-dichlorofluorescein diacetate (DCFH-DA) kit were purchased from

Thermo Scientific (USA). Mitochondrial Membrane Potential Assay Kit with JC-1 was purchased from Abbkine Biotechnology (China). GSH Assay Kit was purchased from Abcam (UK). MDA Assay Kit was purchased from Abnova (China). Calreticulin (D3E6) XP® Rabbit mAb, HMGB1 Antibody, Anti-rabbit IgG (H + L), F (ab')2 Fragment (Alexa Fluor® 647 Conjugate), and DAPI were purchased from Cell Signaling Technology (USA).

4.2. Synthesis of ligands and complexes

4.2.1. Preparation of compound **5a**

To a mixed solution of compound **4** (1.048 g, 4 mmol), 4-methylpiperidine (0.372 g, 4 mmol) and K_2CO_3 (0.553 g, 4 mmol) in MeCN (20 mL) was added 1–2 drops of DMF. After stirring at 85 °C for 12 h, the solution was extracted with DCM (40 mL × 3). The combined organic layers were dried with anhydrous Na_2SO_4 and evaporated to afford crude product, which was finally purified by column chroma-tography using ammonia MeOH/DCM (1:15, v/v) as the eluent to afford 4-methyl-4'-((4-methylpiperidin-1-yl)methyl)-2,2′-bipyridine (**5a**) as light yellow solid (0.933 g, 83 %). ^{1}H NMR (400 MHz, $CDCl_3$) δ 8.61 (d, J = 5.0 Hz, 1H, ArH), 8.54 (d, J = 4.9 Hz, 1H, ArH), 8.29 (d, J = 1.6 Hz, 1H, ArH), 8.22 (d, J = 1.7 Hz, 1H, ArH), 7.36 (dd, J = 5.0, 1.7 Hz, 1H, ArH), 7.13 (dd, J = 5.0, 1.7 Hz, 1H, ArH), 3.56 (s, 2H, CH_2), 2.85 (m, 2H, CH_2), 2.44 (s, 3H, CH_3), 2.01 (m, 2H, CH_2), 1.60 (m, 2H, CH_2), 1.28 (m, 3H, CH_2, CH), 0.92 (d, J = 6.1 Hz, 3H, CH_3). ^{13}C NMR (101 MHz, $CDCl_3$) δ 156.16, 156.08, 149.31, 149.10, 148.98, 148.12, 124.64, 123.98, 122.06, 121.54, 62.42, 54.12, 34.29, 30.64, 21.90, 21.20. HRMS(ESI) m/z Calcd for $C_{18}H_{23}N_3$ $[M + H]^+$, 282.1970; found, 282.1962.

4.2.2. Preparation of compound **5b**

Referring to the method of compound **5a**, 4-methylpiperidine was replaced with 1,4′-bipiperidine to obtain 1'-((4′-methyl-[2,2′-bipyridin]-4-yl)methyl)-1,4′-bipiperidine (**5b**) as light yellow solid (80 %). ^{1}H NMR (400 MHz, $CDCl_3$) δ 8.53 (d, J = 5.0 Hz, 1H, ArH), 8.46 (d, J = 5.0 Hz, 1H, ArH), 8.22 (d, J = 1.6 Hz, 1H, ArH), 8.15 (d, J = 1.6 Hz, 1H, ArH), 7.26 (m, 1H, ArH), 7.05 (m, 1H, ArH), 3.48 (s, 2H, CH_2), 2.86 (m, 2H, CH_2), 2.42 (m, 4H, $2CH_2$), 2.36 (s, 3H, CH_3), 2.17 (m, 1H, CH), 1.94 (m, 2H, CH_2), 1.69 (m, 2H, CH_2), 1.60–1.47 (m, 6H, $3CH_2$), 1.35 (m, 2H, CH_2). ^{13}C NMR (101 MHz, $CDCl_3$) δ 156.22, 156.04, 149.25, 149.12, 148.98, 148.10, 124.65, 123.82, 122.04, 121.39, 62.62, 61.97, 53.65, 50.23, 27.91, 26.42, 24.81, 21.19. HRMS(ESI) m/z Calcd for $C_{22}H_{30}N_4$ $[M + H]^+$, 351.2549; found, 351.2544.

4.2.3. Preparation of compound **5c**

Referring to the method of compound **5a**, 4-methylpiperidine was replaced with piperidin-4-one to obtain 1-((4′-methyl-[2,2′-bipyridin]-4-yl)methyl)piperidin-4-one (**5c**) as light yellow solid (77 %). ^{1}H NMR (400 MHz, $CDCl_3$) δ 8.57 (d, J = 5.0 Hz, 1H, ArH), 8.47 (d, J = 5.0 Hz, 1H, ArH), 8.30 (d, J = 1.6 Hz, 1H, ArH), 8.17 (d, J = 1.7 Hz, 1H, ArH), 7.31 (dd, J = 4.9, 1.7 Hz, 1H, ArH), 7.08 (dd, J = 5.0, 1.7 Hz, 1H, ArH), 3.64 (s, 2H, CH_2), 2.72 (m, 4H, $2CH_2$), 2.42 (m, 4H, $2CH_2$), 2.37 (s, 3H, CH_3). ^{13}C NMR (101 MHz, $CDCl_3$) δ 207.72, 155.50, 154.79, 148.30, 147.98, 147.55, 147.22, 123.80, 122.55, 121.06, 120.13, 59.94, 52.12, 40.23, 20.18. HRMS(ESI) m/z Calcd for $C_{17}H_{19}N_3O$ $[M + H]^+$, 282.1606; found, 282.1601.

4.2.4. Preparation of compound **5d**

Referring to the method of compound **5a**, 4-methylpiperidine was replaced with 1-benzylpiperazine to obtain 4-((4-benzylpiperazin-1-yl)methyl)-4′-methyl-2,2′-bipyridine (**5d**) as yellow solid (74 %). ^{1}H NMR (400 MHz, $CDCl_3$) δ 8.60 (d, J = 5.0 Hz, 1H, ArH), 8.54 (d, J = 5.0 Hz, 1H, ArH), 8.30 (d, J = 1.6 Hz, 1H, ArH), 8.22 (d, J = 1.7 Hz, 1H, ArH), 7.36–7.31 (m, 4H, 4ArH), 7.25 (m, 2H, 2ArH), 7.13 (dd, J = 5.0, 1.7 Hz, 1H, ArH), 3.59 (s, 2H, CH_2), 3.54 (s, 2H, CH_2), 2.48 (m, 11H, CH_3, $4CH_2$). ^{13}C NMR (101 MHz, $CDCl_3$) δ 156.29, 155.98, 149.16, 148.99, 148.69, 148.15, 137.70, 129.33, 129.08, 128.38, 128.25, 127.36, 127.15, 124.71, 123.95, 122.07, 121.51, 62.93, 61.89, 53.06, 52.92, 21.21. HRMS(ESI) m/z Calcd for $C_{23}H_{26}N_4$ $[M + H]^+$, 359.2236; found, 359.2237.

4.2.5. Preparation of compound **5e**

Referring to the method of compound **5a**, 4-methylpiperidine was replaced with 1-phenylpiperazine to obtain 4-methyl-4'-((4-phenylpiperazin-1-yl)methyl)-2,2′-bipyridine (**5e**) as yellow solid (71 %). ^{1}H NMR (400 MHz, $CDCl_3$) δ 8.64 (d, J = 5.0 Hz, 1H, ArH), 8.55 (d, J = 5.0 Hz, 1H, ArH), 8.35 (s, 1H, ArH), 8.24 (s, 1H, ArH), 7.41 (s, 1H, ArH), 7.31–7.22 (m, 2H, 2ArH), 7.15 (d, J = 3.3 Hz, 1H, ArH), 6.93 (d, J = 8.2 Hz, 2H, 2ArH), 6.86 (m, 1H, ArH), 3.67 (s, 2H, CH_2), 3.23 (m, 4H, $2CH_2$), 2.67 (m, 4H, $2CH_2$), 2.45 (s, 3H, CH_3). ^{13}C NMR (101 MHz, $CDCl_3$) δ 156.40, 155.93, 151.28, 149.28, 149.03, 148.22, 129.13, 124.79, 123.98, 122.09, 121.54, 119.78, 116.13, 61.94, 53.24, 49.12, 21.24. HRMS(ESI) m/z Calcd for $C_{22}H_{24}N_4$ $[M + H]^+$, 345.2079; found, 345.2078.

4.2.6. Preparation of complex **6a**

A solution of **5a** (0.421 g, 1.5 mmol) and $RuCl_3 \cdot H_2O$ (0.103 g, 0.5 mmol) in ethylene glycol (5 mL) was stirred for 6 h at 120 °C. Then three steaming water (40 mL) and NH_4PF_6 (0.744 g, 4 mmol) were added and then stirred at room temperature for another 10 min. The reaction was filtered and washed with three steaming water (5 mL × 3) and chloroform (10 mL × 3). The crude product was purified by column chromatography with ammonia MeOH/DCM (1:20, v/v) as the eluent to obtain target compound **6a** as orange-red solid (0.321 g, 52 %). ^{1}H NMR (400 MHz, DMSO-d_6) δ 8.68 (s, 6H, 6ArH), 7.74–7.61 (m, 3H, 3ArH), 7.59–7.51 (m, 3H, 3ArH), 7.46 (d, J = 5.8 Hz, 3H, 3ArH), 7.39–7.33 (m, 3H, 3ArH), 3.66 (s, 6H, $3CH_2$), 2.97–2.61 (m, 6H, $3CH_2$), 2.53 (s, 9H, $3CH_3$), 1.59 (s, 6H, $3CH_2$), 1.43–1.29 (m, 6H, $3CH_2$), 1.22 (s, 9H, $3CH_2$, 3CH), 0.90 (d, J = 6.2 Hz, 9H, $3CH_3$). ^{13}C NMR (101 MHz, DMSO-d_6) δ 156.90, 156.53, 151.33, 150.75, 149.97, 129.01, 125.57, 124.29, 53.89, 34.24, 30.40, 22.22, 21.15. HRMS(ESI) m/z Calcd for $C_{54}H_{69}N_9Ru$ $[M\text{-}2PF_6]^{2+}$, 472.7360; found, 472.7365.

4.2.7. Preparation of complex **6b**

Referring to the method of compound **6a**, **5a** was replaced with **5b** to obtain target compound **6b** as orange-red solid (55 %). ^{1}H NMR (400 MHz, DMSO-d_6) δ 8.77–8.57 (m, 6H, 6ArH), 7.70–7.48 (m, 6H, 6ArH), 7.48–7.41 (m, 3H, 3ArH), 7.39–7.32 (m, 3H, 3ArH), 3.69 (s, 6H, $3CH_2$), 3.19 (d, J = 12.6 Hz, 3H, 3CH), 3.03–2.83 (m, 12H, $6CH_2$), 2.52 (s, 9H, $3CH_3$), 2.16–1.61 (m, 36H, $18CH_2$), 1.52–1.28 (m, 6H, $3CH_2$). ^{13}C NMR (101 MHz, DMSO-d_6) δ 156.92, 156.88, 156.45, 151.26, 150.71, 150.01, 129.03, 127.58, 125.50, 124.19, 62.98, 59.98, 52.01, 49.60, 26.16, 23.33, 21.87, 21.11. HRMS(ESI) m/z Calcd for $C_{66}H_{90}N_{12}Ru$ $[M\text{-}2PF_6]^{2+}$, 576.3228; found, 576.3239.

4.2.8. Preparation of complex **6c**

Referring to the method of compound **6a**, **5a** was replaced with **5c** to obtain target compound **6c** as orange-red solid (53 %). ^{1}H NMR (400 MHz, DMSO-d_6) δ 8.73–8.69 (m, 3H, 3ArH), 8.68–8.65 (m, 3H, 3ArH), 7.70–7.51 (m, 6H, 6ArH), 7.48 (d, J = 5.9 Hz, 3H, 3ArH), 7.38–7.34 (m, 3H, 3ArH), 3.86 (s, 12H, $6CH_2$), 3.72 (s, 6H, $3CH_2$), 2.53 (s, 9H, $3CH_3$), 1.67 (d, J = 5.6 Hz, 12H, $6CH_2$). ^{13}C NMR (101 MHz, DMSO-d_6) δ 156.89, 156.51, 151.27, 150.70, 149.96, 129.00, 127.52, 125.56, 124.07, 106.59, 64.09, 60.16, 51.50, 34.81, 21.12. HRMS(ESI) m/z Calcd for $C_{51}H_{57}N_9O_3Ru$ $[M\text{-}2PF_6 + 3CH_3CHO]^{2+}$, 538.7207; found, 538.7210.

4.2.9. Preparation of complex **6d**

Referring to the method of compound **6a**, **5a** was replaced with **5d** to obtain target compound **6d** as orange-red solid (51 %). ^{1}H NMR (400 MHz, DMSO-d_6) δ 8.79–8.61 (m, 6H, 6ArH), 7.70–7.48 (m, 6H, 6ArH), 7.44 (d, J = 6.0 Hz, 3H, 3ArH), 7.38–7.21 (m, 18H, 18ArH), 3.67 (d, J = 3.5 Hz, 6H, $3CH_2$), 3.55–3.41 (m, 6H, $3CH_2$), 2.51 (s, 12H, $6CH_2$), 2.42

(s, 21H, $3CH_3$, $3CH_2$). ^{13}C NMR (101 MHz, DMSO-d_6) δ 156.86, 156.50, 151.26, 150.71, 150.39, 149.94, 129.33, 129.01, 128.66, 127.67, 127.46, 125.56, 124.29, 62.48, 60.66, 53.25, 52.87, 21.14. HRMS(ESI) *m/z* Calcd for $C_{69}H_{78}N_{12}Ru$ $[M\text{-}2PF_6]^{2+}$, 588.2758; found, 588.2777.

4.2.10. Preparation of complex **6e**

Referring to the method of compound **6a**, **5a** was replaced with **5e** to obtain target compound **6e** as orange-red solid (57 %). ^1H NMR (400 MHz, DMSO-d_6) δ 8.79–8.67 (m, 6H, 6ArH), 7.75–7.49 (m, 9H, 9ArH), 7.37 (d, $J = 5.8$ Hz, 3H, 3ArH), 7.25–7.15 (m, 6H, 6ArH), 6.98–6.90 (m, 6H, 6ArH), 6.82–6.73 (m, 3H, 3ArH), 3.80–3.67 (m, 6H, $3CH_2$), 3.23–3.11 (m, 12H, $6CH_2$), 2.66–2.56 (m, 12H, $6CH_2$), 2.53 (s, 9H, $3CH_3$). ^{13}C NMR (101 MHz, DMSO-d_6) δ 156.94, 156.55, 151.39, 150.78, 150.28, 149.99, 129.42, 129.05, 127.77, 125.63, 124.33, 119.41, 115.88, 60.64, 53.21, 48.60, 21.15. HRMS(ESI) *m/z* Calcd for $C_{66}H_{72}N_{12}Ru$ $[M\text{-}2PF_6]^{2+}$, 567.2523; found, 567.2528.

4.3. Lipophilicity

The lipophilicity of RuB and **6a-e** was assessed through the determination of their octanol-water partition coefficients, denoted as log P, employing a previously documented methodology [49].

4.4. The absorption and fluorescence spectra

The stock solution of **6a-e** in DMSO (5 mM) was appropriately diluted with methanol to achieve the desired working concentration (10 μM). Spectral scanning was carried out using 3 mL of the prepared solution in cuvettes. For the emission spectrum scans, the complexes were excited at a wavelength of 460 nm.

4.5. In vitro ROS, $\bullet O^{2-}$, and •OH detection

Firstly, prepare stock solutions (5 mM) of DCFH or **6a-e** in DMSO. Then, add a specific volume of each stock solution into 3 mL of methanol to achieve a uniform concentration of 10 μM for each. Then, the probe DCFH-DA, DHE, or HPF was added to the methanol solution to achieve the desired working concentration (10 μM). All procedures are conducted under light-protected conditions. The fluorescence spectrum was measured at different irradiation (520 nm, 200 mW/cm^2) time.

4.6. Calculation of $^1O_2$ quantum yield (Φ_Δ)

DPBF was utilized as the detection agent for the measurement of the Φ_Δ. The absorbance of DPBF in methanol was adjusted to approximately 1.0 at 415 nm. To minimize the $^1O_2$ quenching by RuB and **6a-e** themselves, their absorbance at 520 nm were adjusted to below 0.1. All procedures are conducted under light-protected conditions. The decomposition rates of DPBF by the Ru(II) complexes were monitored at different irradiation (520 nm, 200 mW/cm^2) times, with the absorbance changes of DPBF at 412 nm utilized for quantification of Φ_Δ. Using RuB ($\Phi_\Delta = 0.73$, in methanol) as a reference. The Φ_Δ of the samples were calculated according to the following equation:

$$\Phi_{\Delta(X)} = \Phi_{\Delta(S)} (k_X \times F_S) / (k_S \times F_X)$$

where *k* denotes the calibrated slope of the linear fit of the cumulative decrease of the absorbance at 415 nm versus the change of irradiation time. F denotes the correction factor calculated using equation 2. S denotes the samples awaiting testing, and X denotes the reference, that is, RuB.

$$F = 1 - 10^{-OD}$$

where *OD* denotes the amount of light absorbed by the mixture at 520 nm.

4.7. Calculation of fluorescence quantum yield (Φ_F)

Using **RuB** ($\Phi_F = 0.328$, in a mixture of methanol and ethanol (1:4, v/v)) as a reference, Φ_F of **6a** and **6d** were determined in the same solvent. Φ_F was calculated according to the following equation 3 reported in the literature [36].

$$\Phi_{F(X)} = \Phi_{F(S)} (A_S F_X / A_X F_S) (n_X / n_S)^2$$

where F denotes the integrated area of fluorescence spectrum at the same excitation wavelength. A denotes the absorbance values at the excitation wavelength. N denotes the refractive index of the solvents. S denotes the samples awaiting testing, and X denotes the reference, that is, RuB. ($n_X/n_S = 1$ in this work).

4.8. Photostability study

The stock solution of **6a**/**6d** in DMSO (5 mM) was appropriately diluted with methanol to achieve the desired working concentration (20 μM). The UV–vis absorption spectrum was measured at different irradiation (520 nm, 200 mW/cm^2) times.

4.9. Electron paramagnetic resonance (EPR) assay

The EPR assay were conducted using an electron spin resonance spectrometer at 298 K. The type of ROS was identified using the $\bullet O_2^-$ scavenger 5,5-dimethyl-1-pyrroline N-oxide (DMPO), •OH scavenger 2,2,6,6-tetramethyl-4-nitropiperidine oxide (TNPO) and $^1O_2$ scavenger 2,2,6,6–tetramethylpiperidine (TEMP). Light source: 10 min, 520 nm, and 200 mW/cm^2.

4.10. Cell culture and in vitro cytotoxicity assay

All cell lines used in this study, including HT29, A549, and 4T1, were sourced from the Shanghai Institute of Cell Biology (China). All cells were cultured under carefully controlled conditions at a constant temperature of 37 °C with a 5 % CO_2 atmosphere. They were routinely incubated in dulbecco's modified eagle medium (DMEM) that was supplemented with 10 % fetal bovine serum (FBS).

The MTT assay was employed to determine the *in vitro* cytotoxicities of complexes **6a-e**. HT29, A549, and 4T1 cells were seeded in 96-well microplate at a density of 1×10^5 cells/mL in 100 μL culture medium containing 10 % FBS and incubated for 12 h. Different concentrations (2, 5, 10, 20, 40, and 100 μM) of the complexes were added individually to the culture media and incubated for another 12 h under normoxic or hypoxic condition. The supernatant was replaced with a fresh culture medium, and the cells were subjected to irradiation (520 nm, 200 mW/cm^2) for 10 min, and incubated for an additional 24 h in the dark. Cells in the non-irradiation group were replaced with a fresh culture medium and maintained in the dark. MTT solution (10 μL, 5 mg/mL in PBS) was added to each well, and the cells were further incubated for 3 h. Afterward, the culture medium were removed and 100 μL of DMSO solution was added to each well to dissolve the formazan crystals. The absorbance values at 570 nm were then measured using a multifunction microplate reader, and the corresponding cell viability was determined based on the data obtained.

4.11. Live/dead cell stain

Cells were seeded on confocal dishes at a density of 1×10^5 cells/mL in 2.0 mL culture medium and allowed to adhere upon incubation for 12 h. Following removal of the culture medium, the cells were subjected to various treatments: (control, L, **6d**/**6a** (10 μM), and **6d**/**6a** (10 μM) + L) and further incubated for 4 h. The cells were stained with PI (60 μg/mL) and Calcein-AM (100 μg/mL) in PBS for 30 min. The fluorescence images were obtained immediately using a confocal microscope. Light

dose: 520 nm, 200 mW/cm^2, 10 min.

4.12. Cellular co-localization assay

Cells were seeded on confocal dishes at a density of 2×10^5 cells/mL in 2.0 mL culture medium and allowed to adhere overnight. Subsequently, the cells were treated with **6d**/**6a** (10 μM) for 4 h at 37 °C in the absence of light. Following this incubation period, the cells were washed with phosphate-buffered saline. Next, the cells were further incubated with either LysoTracker Green (1 μM) or Mito-Tracker Green (75 nM) for 30 min at 37 °C in the dark. The cells were washed three times with phosphatebuffered saline to remove excess dye. Confocal images were acquired using a confocal microscope to visualize the localization of the complexes within the cells. Mito-Tracker Green: λ_{ex} = 460 nm, λ_{em} = 505–525 nm; **6a**: λ_{ex} = 459 nm, λ_{em} = 600–650 nm; **6d**: λ_{ex} = 460 nm, λ_{em} = 600–650 nm. Lyso-tracker Green: λ_{ex} = 460 nm, λ_{em} = 490–520 nm; **6a**: λ_{ex} = 459 nm, λ_{em} = 620–670 nm; **6d**: λ_{ex} = 460 nm, λ_{em} = 620–670 nm.

4.13. Intracellular ROS detection

Intracellular generation of ROS was visualized using fluorescence imaging with a DCFH-DA probe. Following a 24 h incubation and removal of the culture medium, the PBS group was set aside. Cells were then treated with **6a**/**d** (10 μM) and incubated for 4 h. After that, DCFH-DA (10 μM) was added as a ROS detection reagent, and the cells were incubated for another 30 min. The cells in the light group were subjected to irradiation with a 520 nm laser (200 mW/cm^2, 10 min). The fluorescence images were then obtained using a confocal microscope.

4.14. Mitochondrial membrane potential (MMP) detection

Cells were seeded on confocal dishes at a density of 1×10^5 cells/mL in 2.0 mL culture medium and allowed to adhere upon incubation for 12 h. Following removal of the culture medium, the cells were subjected to various treatments: (control, L, **6d**/**6a** (10 μM), and **6d**/**6a** (10 μM) + L) and further incubated for 4 h. Next, the cells were further incubated with JC-1 solution (10 μg/mL) for 20 min at 37 °C. The fluorescence images were obtained immediately using a confocal microscope. Light dose: 520 nm, 200 mW/cm^2, 10 min. Green channel: E_x, 488 nm; E_m, 510–545 nm; Red channel: E_x: 535 nm; E_m: 580–610 nm.

4.15. Intracellular malondialdehyde (MDA) level detection

A549 cells were seeded in a six-well plate with fresh DMEM containing 10 % FBS (2.0 mL per well) and incubation for 24 h. Following incubation, the cells were subjected to various treatments: (control, L, RuB (10 μM), RuB (10 μM) + L, **6d** (10 μM), **6d** (10 μM) + L, **6d** (10 μM) + Fer-1 (1 μM), and **6d** (10 μM) + Fer-1 (1 μM) + L) and further incubated for 24 h. Then the culture medium was removed, and the cells were lysed to collect the cell lysate. Subsequently, the concentration of MDA content was measured using a standard MDA assay kit. The absorbance of the supernatants was measured using a multifunction microplate reader at wavelengths of 532 nm and 600 nm according to the provided equation.

$$\Delta OD = OD(Test) - OD(Blank)$$

$$MDA\ (nmol/10^4\ cell) = 0.1075 \times (\Delta OD_{532\ nm} - \Delta OD_{600\ nm})$$

where OD denotes the absorbance values at the excitation wavelength.

4.16. Intracellular GSH level detection

A549 cells were seeded in a six-well plate with fresh DMEM containing 10 % FBS (2.0 mL per well) and incubation for 48 h. Following incubation, the cells were subjected to various treatments: (control, L, RuB (10 μM), RuB (10 μM) + L, **6d** (10 μM), and **6d** (10 μM) + L) and further incubated for 24 h. Then the culture medium was removed, and the cells were lysed to collect the cell lysate. Subsequently, the concentration of GSH content was measured using a GSH assay kit according to the manufacturer's instructions (Beyotime).

4.17. Western blot analysis

Briefly, A549 cells were seeded in a six-well plate with fresh DMEM containing 10 % FBS (2.0 mL per well) and incubation for 24 h. Following incubation, the cells were subjected to various treatments: (control, L, **6d** (10 μM), and **6d** (10 μM) + L) and further incubated for 24 h. After being washed twice with cold DPBS, the A549 cells were treated with of ice-cold lysis buffer (60 μL). Upon disruption, the cell lysate was collected and boiled for 300 s at 95 °C. Subsequently, the cell lysates underwent SDS-polyacrylamide gel electrophoresis (SDS-PAGE) and a polyvinylidene fluoride (PVDF) membrane was used to transfer protein. The PVDF membrane was then blocked with skim milk (5 % TBST). Following this, the membrane was immunoblotted with a Glutathione Peroxidase 4 (GPX4) rabbit polyclonal antibody (dilution: 1:1000) and an *anti*-β-actin antibody (dilution: 1:2000) for 15 h. Subsequently, the membrane was incubated with secondary antibody (dilution: 1:10,000) coupled with peroxidase (HRP) for another 1.5 h. Finally, specific protein bands were captured using an Omega Lum C Imaging System.

4.18. Detection of lipid peroxidation

Lipid peroxidation of **6d** was visualized using fluorescence imaging using the C11-BODIPY 581/591 probe. Following a 24 h incubation and removal of the culture medium, the cells were subjected to various treatments: (control, L, **6d**/RuB (10 μM), and **6d**/RuB (10 μM) + L) and further incubated for 4 h. Subsequently, the cells were washed with PBS and treated with C11-BODIPY (5 μM) for 30 min. Fluorescence imaging was conducted using conventional filters: Texas Red (581/591 nm) and FITC (488/510 nm). Simultaneously, data acquisition for oxidized BODIPY was efficiently carried out at its excitation maximum of 488 nm and emission maximum of 510 nm.

4.19. Cell death mechanism

To investigate the cell death mechanism, the cell viability was assessed following preincubation with various inhibitors targeting different cell death pathways. Cells were seeded in a 96 well plate at a density of 1×10^5 cells/mL in 2.0 mL culture medium and allowed to adhere upon incubation for 24 h. Preincubation with 3-Methyladenine (100 μM), Ferrostatin-1 (10 μM), Necrostatin-1 (50 μM) or *Z*-VAD-FMK (5 μM) were carried out for 60 min. Subsequently, **6d** (10 μM) was added and incubated for 4 h. Afterward, the cells were washed and subjected to irradiation (520 nm, 200 mW/cm^2, 10 min). Cells in the non-irradiation group were replaced with fresh culture medium and kept in the dark. After an additional 20 h of co-incubation, with or without the respective inhibitors, the survival rate of A549 cells was determined using the MTT assay.

4.20. Immunofluorescence staining of calreticulin (CRT)

Following incubation with **6d** (10 μM) for 4 h, the supernatant was refreshed with fresh culture medium prior to irradiation. Following an additional 20 h incubation, cells were subjected to staining usin CRT (D3E6) XP® Rabbit mAb, Anti-Rabbit IgG (H + L), F (ab')2 Fragment (Alexa Fluor® 647 Conjugate), and DAPI for 15 min following PBS washing. Subsequently, confocal microscopy was employed to image the slides, with excitation at 633 nm and emission collected at 690 ± 40 nm. The specific operation is to refer to the method in the literature [50].

4.21. Immunofluorescence staining of extracellular HMGB1

The cell treatment mirrored that of the CRT experiment. Instead of CRT (D3E6) XP® Rabbit mAb, HMGB1 Antibody was utilized. Confocal microscopy was employed to image the cells, with excitation at 514 nm and emission collected at 620 ± 20 nm.

4.22. Extracellular ATP detection assay

The protocol for detecting extracellular ATP involved employing the ATP Bioluminescence Detection Kit (Promega). Post-collection, 100 μL of supernatant was mixed with an equivalent volume of reagents in opaque-walled plates. Subsequent quantification of ATP chemiluminescence signals was carried out using the TECAN Infinite M200 PRO multifunctional reader. Correction of actual ATP content values across groups was conducted to adjust for differences in cell viability under varied culture conditions.

4.23. Tumor mice model

All animal experiments were conducted in accordance with the guidelines and regulations set forth by the Animal Research and Care Committee of Nantong University (Approval No.: S20210925-003). For the establishment of the tumor-bearing mouse model, female BALB/c nude mice (5–6 week), with an average weight of around 20 g, were used. A suspension containing 5×10^5 A549 or 4T1 cells in PBS buffer was subcutaneously injected into each mouse. After approximately 9 days, mice with tumor volumes reaching approximately 100 mm^3 were selected for further experimentation.

4.24. In vivo antitumor efficacy

The therapeutic efficacy was evaluated via intratumoral (i.t.) injection. Once the tumors reached approximately 100 mm^3, the mice were randomly divided into four groups (n = 3 per group): "PBS", "RuB + L", "**6d**/**6a**", and "**6d**/**6a** + L". Each group received an i. t. Injection of 200 μL of the respective treatment: PBS alone, RuB (5 mg/kg), **6d**/**6a** (5 mg/kg), or **6d**/**6a** (5 mg/kg). 4 h post-injection, the "RuB + L″ and "**6d**/**6a** + L" groups underwent irradiation at 520 nm (200 mW/cm^2) for 10 min. Throughout the subsequent 21-day period, the body weight and tumor volume of the mice were measured every 3 days. Tumor volume (V) was calculated using formula $V = a \times b^2/2$ (where a represents tumor length and b represents tumor width). After the 21-day treatment period, all mice were euthanized. Major organs (heart, liver, spleen, lung, kidney), along with tumors, were collected and subjected to hematoxylin and eosin (H&E) staining to assess morphological changes.

4.25. Statistical analyses

All data were presented as mean ± standard deviation (s.d.). Statistical significance was analyzed using a Student's t-test or two-way analysis of variance (ANOVA). All origin graphs were drawn with OriginLab Origin 2021.

CRediT authorship contribution statement

Hongwei Zheng: Writing – original draft, Investigation. **Kai Wang:** Software, Resources. **Dongliang Ji:** Software, Resources. **Xiao Liu:** Investigation. **Chen Wang:** Resources. **Yangyang Jiang:** Software. **Zihan Jia:** Resources. **Biao Xiong:** Methodology, Investigation. **Yong Ling:** Writing – review & editing, Project administration, Methodology. **Jiefei Miao:** Writing – review & editing, Methodology.

Declaration of competing interest

The authors declare that they have no known competing financial interests or personal relationships that could have appeared to influence the work reported in this paper.

Data availability

Data will be made available on request.

Acknowledgments

This work was supported by the National Natural Science Foundation of China (21977058 and 82473840); Key R&D Program of Jiangsu Province (BE2021677); China Postdoctoral Science Foundation (2018T110533); Key Natural Science Foundation of Jiangsu Higher Education Institutions (20KJA350002); and Jiangsu Province Innovation Project of Postgraduate Training (KYCX22_3380 and KYCX24_3559).

Appendix A. Supplementary data

Supplementary data to this article can be found online at https://doi.org/10.1016/j.ejmech.2024.116909.

References

[1] A. Jassim, E.P. Rahrmann, B.D. Simons, R.J. Gilbertson, Cancers make their own luck: theories of cancer origins, Nat. Rev. Cancer 23 (2023) 710–724.
[2] C. Thakur, F. Chen, Connections between metabolism and epigenetics in cancers, Semin. Cancer Biol. 57 (2019) 52–58.
[3] L. Zhao, C. Gu, Y. Gan, L. Shao, H. Chen, H. Zhu, Exosome-mediated siRNA delivery to suppress postoperative breast cancer metastasis, J. Contr. Release 318 (2020) 1–15.
[4] P. Kalluru, M. Shanmugam, R. Vankayala, C.-S. Chiang, K.C. Hwang, Conquering multidrug resistant lung cancer by upconversion nanoparticles-mediated photodynamic therapy and gene silencing, J. Chin. Chem. Soc. 69 (2022) 1305–1317.
[5] A. Leiter, R.R. Veluswamy, J.P. Wisnivesky, The global burden of lung cancer: current status and future trends, Nat. Rev. Clin. Oncol. 20 (2023) 624–639.
[6] A. Tulpule, T.G. Bivona, Acquired resistance in lung cancer, Annu. Rev. Cell Biol. 4 (2020) 279–297.
[7] X. Zheng, X. Song, G. Zhu, D. Pan, H. Li, J. Hu, K. Xiao, Q. Gong, Z. Gu, K. Luo, W. Li, Nanomedicine combats drug resistance in lung cancer, Adv. Mater. 36 (2024) e2308977.
[8] K. Wang, B. Yu, J.L. Pathak, An update in clinical utilization of photodynamic therapy for lung cancer, J. Cancer 12 (2021) 1154–1160.
[9] G. Chen, Y. Zhao, Y. Xu, C. Zhu, T. Liu, K. Wang, Chitosan nanoparticles for oral photothermally enhanced photodynamic therapy of colon cancer, Int. J. Pharm. 589 (2020) 119763.
[10] S. Zeng, Z. Guo, Y. Hao, Y.S. Kafuti, Z. Yang, Q. Yao, J. Wang, X. Peng, H. Li, Tumor-microenvironment-activatable organic phototheranostic agents for cancer therapy, Coord. Chem. Rev. 509 (2024) 215786.
[11] N.S. James, R.R. Cheruku, J.R. Missert, U. Sunar, R.K. Pandey, Measurement of cyanine dye photobleaching in photosensitizer cyanine dye conjugates could help in optimizing light dosimetry for improved photodynamic therapy of cancer, Molecules 23 (2018) 1842.
[12] D. Chen, Q. Xu, W. Wang, J. Shao, W. Huang, X. Dong, Type I photosensitizers revitalizing photodynamic oncotherapy, Small 17 (2021) e2006742.
[13] Y. Wang, J. Liao, Y. Lyu, Q. Guo, Z. Zhu, X. Wu, J. Yu, Q. Wang, W.-H. Zhu, An AIE photosensitizer with simultaneous type I and type II ROS generation: efficient bacterial elimination and hypoxic tumor ablation, Adv. Funct. Mater. 33 (2023) 2301692.
[14] W. Shen, G. Han, L. Yu, S. Yang, X. Li, W. Zhang, P. Pei, Combined prussian blue nanozyme carriers improve photodynamic therapy and effective interruption of tumor metastasis, Int. J. Nanomed. 17 (2022) 1397–1408.
[15] J. Zhang, C. Jiang, J.P. Figueiro Longo, R.B. Azevedo, H. Zhang, L.A. Muehlmann, An updated overview on the development of new photosensitizers for anticancer photodynamic therapy, Acta Pharm. Sin. B 8 (2018) 137–146.
[16] M. Wainwright, Photodynamic therapy: the development of new photosensitisers, Anti Cancer Agents Med. Chem. 8 (2008) 280–291.
[17] H. Abrahamse, M.R. Hamblin, New photosensitizers for photodynamic therapy, Biochem. J. 473 (2016) 347–364.
[18] D. Chen, M. Song, J. Huang, N. Chen, J. Xue, M. Huang, Photocyanine: a novel and effective phthalocyanine-based photosensitizer for cancer treatment, J Innov Opt Heal Sci 13 (2020) 2030009.
[19] J. Chen, Y. Xu, Y. Gao, D. Yang, F. Wang, L. Zhang, B. Bao, L. Wang, Nanoscale organic-inorganic hybrid photosensitizers for highly effective photodynamic cancer therapy, ACS Appl. Mater. Interfaces 10 (2018) 248–255.
[20] G. Murali, B. Kwon, H. Kang, J.K.R. Modigunta, S. Park, S. Lee, H. Lee, Y.H. Park, J. Kim, S.Y. Park, Y.-J. Kim, I. In, Hematoporphyrin photosensitizer-linked carbon

quantum dots for photodynamic therapy of cancer cells, ACS Appl. Nano Mater. 5 (2022) 4376–4385.
[21] P. Bhattarai, Z. Dai, Cyanine based nanoprobes for cancer theranostics, Adv. Healthcare Mater. 6 (2017) 1700262.
[22] L. Wei, X. He, D. Zhao, M. Kandawa-Shultz, G. Shao, Y. Wang, Biotin-conjugated Ru(II) complexes with AIE characteristics as mitochondria-targeted photosensitizers for enhancing photodynamic therapy by disrupting cellular redox balance, Eur. J. Med. Chem. 264 (2024) 115985.
[23] J. Karges, F. Heinemann, M. Jakubaszek, F. Maschietto, C. Subecz, M. Dotou, R. Vinck, O. Blacque, M. Tharaud, B. Goud, E. Vinuelas ZahiNos, B. Spingler, I. Ciofini, G. Gasser, Rationally designed long-wavelength absorbing Ru(II) polypyridyl complexes as photosensitizers for photodynamic therapy, J. Am. Chem. Soc. 142 (2020) 6578–6587.
[24] J. Liu, C. Zhang, T.W. Rees, L. Ke, L. Ji, H. Chao, Harnessing ruthenium(II) as photodynamic agents: encouraging advances in cancer therapy, Coord. Chem. Rev. 363 (2018) 17–28.
[25] H. Huang, B. Yu, P. Zhang, J. Huang, Y. Chen, G. Gasser, L. Ji, H. Chao, Highly charged ruthenium(II) polypyridyl complexes as lysosome-localized photosensitizers for two-photon photodynamic therapy, Angew. Chem. Int. Ed. 54 (2015) 14049–14052.
[26] M. Dickerson, Y. Sun, B. Howerton, E.C. Glazer, Modifying charge and hydrophilicity of simple Ru(II) polypyridyl complexes radically alters biological activities: old complexes, surprising new tricks, Inorg. Chem. 53 (2014) 10370–10377.
[27] A. Bergamo, L. Messori, F. Piccioli, M. Cocchietto, G. Sava, Biological role of adduct formation of the ruthenium(III) complex NAMI-A with serum albumin and serum transferrin, Invest. N. Drugs 21 (2003) 401–411.
[28] C.G. Hartinger, M.A. Jakupec, S. Zorbas-Seifried, M. Groessl, A. Egger, W. Berger, H. Zorbas, P.J. Dyson, B.K. Keppler, KP1019, a new redox-active anticancer agent–preclinical development and results of a clinical phase I study in tumor patients, Chem. Biodivers. 5 (2008) 2140–2155.
[29] P. Heffeter, K. Bock, B. Atil, M.A. Reza Hoda, W. Korner, C. Bartel, U. Jungwirth, B. K. Keppler, M. Micksche, W. Berger, G. Koellensperger, Intracellular protein binding patterns of the anticancer ruthenium drugs KP1019 and KP1339, J. Biol. Inorg. Chem. 15 (2010) 737–748.
[30] S. Monro, K.L. Colon, H. Yin, J. Roque 3rd, P. Konda, S. Gujar, R.P. Thummel, L. Lilge, C.G. Cameron, S.A. McFarland, Transition metal complexes and photodynamic therapy from a tumor-centered approach: challenges, opportunities, and highlights from the development of TLD1433, Chem. Rev. 119 (2019) 797–828.
[31] Y. Lu, D. Zhu, Q. Le, Y. Wang, W. Wang, Ruthenium-based antitumor drugs and delivery systems from monotherapy to combination therapy, Nanoscale 14 (2022) 16339–16375.
[32] C. Parella, A. Blanquer, S. Sinha, E. Hümpfner, J. Hernando, E. Mora, X. Fontrodona, Z. Kelemen, C. Nogués, R. Núñez, I. Romero, Developing photo-activable ruthenium (II) complexes for PDT: synthesis, characterization, photophysical and biological studies, Dyes Pigments 224 (2024) 111985.
[33] J. Karges, H. Chao, G. Gasser, Synthesis, characterization, and biological evaluation of the polymeric encapsulation of a ruthenium(II) polypyridine complex with pluronic F-127/Poloxamer-407 for photodynamic therapy applications, Eur. J. Inorg. Chem. 2020 (2020) 3242–3248.
[34] J. Karges, J. Li, L. Zeng, H. Chao, G. Gasser, Polymeric encapsulation of a ruthenium polypyridine complex for tumor targeted one- and two-photon photodynamic therapy, ACS Appl. Mater. Interfaces 12 (2020) 54433–54444.
[35] L.V. Lutkus, S.S. Rickenbach, T.M. McCormick, Singlet oxygen quantum yields determined by oxygen consumption, J. Photochem. Photobiol. Chem. 378 (2019) 131–135.
[36] J. Liu, X. Liu, J. Qian, C. Meng, P. Zhu, J. Hang, Y. Wang, B. Xiong, X. Qiu, W. Zhu, Y. Yang, Y. Zhang, Y. Ling, Development of pH/glutathione-responsive theranostic agents activated by glutathione S-transferase pi for human colon cancer, J. Med. Chem. 63 (2020) 9271–9283.
[37] R. Zhang, D.-K. Ji, D. Yao, Z. Xiao, W. Tan, Molecular engineering of aptamer to solubilize hydrophobic near-infrared photosensitizer for enhanced cancer photodynamic therapy, CCS Chem. 6 (2024) 1240–1254.
[38] H. Zhang, G. Qi, K. Wang, J. Yang, Y. Shen, X. Yang, X. Chen, X. Yao, X. Gu, L. Qi, C. Zhou, H. Sun, Oxidative stress: roles in skeletal muscle atrophy, Biochem. Pharmacol. 214 (2023) 115664.
[39] X. Wang, Z. Zhang, W. Sun, J. Zhang, Q. Xu, X. Zhou, L. Mao, Ferroptosis in colorectal cancer: potential mechanisms and effective therapeutic targets, Biomed. Pharmacother. 153 (2022) 113524.
[40] D.C. Fuhrmann, B. Brune, A graphical journey through iron metabolism, microRNAs, and hypoxia in ferroptosis, Redox Biol. 54 (2022) 102365.
[41] Y. Zhou, K. Chen, W.K. Lin, J. Liu, W. Kang, Y. Zhang, R. Yang, L. Jin, Y. Cheng, A. Xu, W. Wang, Photo-enhanced synergistic induction of ferroptosis for anti-cancer immunotherapy, Adv. Healthcare Mater. 12 (2023) e2300994.
[42] Y. Zhao, Y. Liu, Y. Xu, K. Li, L. Zhou, H. Qiao, Q. Xu, J. Zhao, The role of ferroptosis in blood-brain barrier injury, Cell. Mol. Neurobiol. 43 (2023) 223–236.
[43] X. Meng, Z. Lu, L. Zhang, Z. Wang, A pH/ATP-responsive nanomedicine via disrupting multipath homeostasis of ferroptosis for enhanced cancer therapy, Chem. Eng. J. 457 (2023) 141313.
[44] Z. Chen, H. Lin, X. Wang, G. Li, N. Liu, M. Zhang, Y. Shen, The application of approaches in detecting ferroptosis, Heliyon 10 (2024) e23507.
[45] A. Ahmed, S.W.G. Tait, Targeting immunogenic cell death in cancer, Mol. Oncol. 14 (2020) 2994–3006.
[46] O. Krysko, T. Love Aaes, C. Bachert, P. Vandenabeele, D.V. Krysko, Many faces of DAMPs in cancer therapy, Cell Death Dis. 4 (2013) e631.
[47] J. Gao, W.Q. Wang, Q. Pei, M.S. Lord, H.J. Yu, Engineering nanomedicines through boosting immunogenic cell death for improved cancer immunotherapy, Acta Pharmacol. Sin. 41 (2020) 986–994.
[48] B.D. Sherman, Y. Xie, M.V. Sheridan, D. Wang, D.W. Shaffer, T.J. Meyer, J. J. Concepcion, Light-driven water splitting by a covalently linked ruthenium-based chromophore–catalyst assembly, ACS Energy Lett. 2 (2017) 124–128.
[49] J.J. Cao, C.P. Tan, M.H. Chen, N. Wu, D.Y. Yao, X.G. Liu, L.N. Ji, Z.W. Mao, Targeting cancer cell metabolism with mitochondria-immobilized phosphorescent cyclometalated iridium(iii) complexes, Chem. Sci. 8 (2017) 631–640.
[50] L. Wang, J. Karges, F. Wei, L. Xie, Z. Chen, G. Gasser, L. Ji, H. Chao, A mitochondria-localized iridium(iii) photosensitizer for two-photon photodynamic immunotherapy against melanoma, Chem. Sci. 14 (2023) 1461–1471.